On the effects of reactant stratification and wall curvature in non-premixed rotating detonation combustors

Venkat Athmanathan[1], James Braun[2], Zachary M. Ayers[2], Christopher Fugger[3], Austin M. Webb[2], Mikhail N. Slipchenko[2,3], Guillermo Paniagua[1,2], Sukesh Roy[3], and Terrence R. Meyer[1,2]

[1] School of Aeronautics and Astronautics, Purdue University, West Lafayette, IN 47907, USA

[2] School of Mechanical Engineering, Purdue University, West Lafayette, IN 47907, USA

[3] Spectral Energies, LLC, 4065 Executive Dr, Beavercreek, OH 45430, USA

Corresponding author:

Dr. Terrence R. Meyer

Maurice J. Zucrow Laboratories, Purdue University

500 Allison Rd.

West Lafayette, IN 47907, USA

trmeyer@purdue.edu

Abstract

The optimization of non-premixed rotating detonation combustors (RDCs) requires improved understanding of the coupled effects of reactant stratification, fluid property gradients, and complex shock-wave interactions on the detonation wave structure within annular geometries. In the current work, simultaneous orthogonal views of chemiluminescence and hydroxyl planar laser-induced fluorescence (PLIF) are utilized to establish the existence of a dual-wave system characterized by leading and trailing detonation waves that are closely coupled by the local flow physics. These features are persistent over a wide range of mass flow rates and are consistent with prior observations of non-premixed rotating detonations in annular geometries. The detailed instantaneous time sequences are compared with a 3D reactive unsteady Reynolds averaged Navier-Stokes (URANS) simulation to more clearly elucidate the *in-situ* combustion dynamics and the sensitivity to reactant inlet conditions. It is found that the dual-wave system results from unburned reactants that survive the leading detonation in the injector near field and are consumed within an azimuthal reflected-shock combustion zone behind leading detonation wave. By contrast, the injector far field is characterized by rapid mixing due to a sudden drop to subsonic conditions, and the bifurcated detonation wave structure collapses into a stronger, single-wave detonation front with higher overall pressure rise as compared with the dual-wave system. While each RDC will have different inflow, mixing, and combustion characteristics, the underlying interactions between the stratified reactants and azimuthal wave dynamics identified through the combination of advanced MHz-rate diagnostics and 3D numerical simulations have important implications for the study of detonation wave stability, mode transition, and combustion efficiency in non-premixed annular RDCs.

1. Introduction

Rotating detonation engines (RDEs) are of significant interest for their potential to achieve pressure-gain combustion in continuous flow devices and to increase thermodynamic efficiency over conventional constant pressure combustion devices with similar fuel-oxidizer combinations [1,2]. Detonative combustion offers the advantage of a highly compact flame and lower compressor loading combined with the ability to be retrofitted in engines for subsonic or supersonic flight. The last two decades have seen extensive research and development of these systems from laboratory-scale engines to practical applications [2–15].

In the vast majority of these rotating detonation combustor (RDC) experiments, the fuel and oxidizer are introduced separately into the combustion channel, leading to reactant stratification and non-ideal detonations [2,16,17]. While the ideal isochoric detonative process is conceptualized using the Chapman-Jouguet (C-J) condition to obtain a theoretical upper bound for the thermodynamic benefit expected [18], inefficiencies arising from inter- and intracycle processes, such as (i) non-ideal mixing of reactants, (ii) deflagrative heat release, and (iii) shock losses from high-speed flow turning in in curved channels, cause a characteristic drop in wave-speed compared to C-J detonations (by as much as 40 %), thus limiting the overall pressure gain [2]. The local detonation wave structure and complex shock reflections in the axial, radial, and azimuthal directions perturb the reactant distribution. Due to the stratified reactant distribution and finite mixing rates, a fraction of the reactants can pass through the detonation wave without combusting, which lowers the thermodynamic performance [19]. Other loss mechanisms that degrade the isochoric heat release process include transverse shock waves reflected from the inlet or exit of the RDC, parasitic deflagration due to contact between fresh reactants with high-temperature products [5,20,21], product expansion following the detonation wave that can alter the injection blockage and recovery pressure, and reactant refill dynamics in the presence of large pressure variations. Detailed understanding of the aforementioned loss mechanisms is important for the development of more efficient RDCs. While numerical simulations of premixed RDCs have been used to study features such as the vitiation of premixed reactants due to mixing with post-detonation products and the role shock-wave reflections [22–26], computations of non-premixed rotating detonation combustors (RDCs) are also needed to capture the coupled effects of reactant stratification and wave stability [19,21,22]. Due to the steep spatio-temporal gradients and effects of finite-rate chemistry, full resolution of the physicochemical processes in non-premixed annular RDCs is not feasible even for simulations with well over 100 million cells and complex chemistry [27,28]. Hence, there is a need for advanced experimental diagnostics that can be used to obtain detailed three-dimensional (3D) information on the detonation wave structure to complement and corroborate practical numerical models.

To understand the propagation of detonation waves through a continuous inflow of reactants, linear channels have been used as so-called ‘unwrapped’ [9,10,28] and ‘rho- RDCs’ [30] with direct optical access to the mixing and combustion zones. These studies allow observation of key features such as the reactant refill height, the oblique shock and triple point locations, and the instantaneous structure of the detonation wave. To provide insight into the physics of wave-initiation specific to continuously spinning detonations present in annular RDCs, researchers have also utilized an obround or “racetrack” geometry in which two hemispherical detonation channels are connected with straight sections with ready optical access forming a closed loop of reactant and product interaction [29–32]. Recent work compared instantaneous hydroxyl planar laser-induced fluorescence (OH-PLIF) imaging from the linear section of an obround RDC with ‘unwrapped’ high-fidelity simulations of an annular RDC [31] to investigate the effects of mixing on the detonation wave propagation. This geometry may also be promising for investigating differences between curved and linear detonation channels, as the fuel and oxidizer are prepared in a similar fashion within each section. However, detailed optical

diagnostics have primarily been reported in the linear portion of the obround combustor. Detonation waves traveling in annular sections, for example, experience flow turning due to the curvature of the channel outer wall, a phenomenon detailed in several numerical and experimental studies [22,33,34]. This flow turning causes an azimuthal wake shock system that can affect the inflow of fresh reactants during the injection recovery. These shock systems specific to annular detonation channels can increase the local static temperature and pressure of the product gas and lead to non-ideal flow losses. In high-speed wall-pressure measurements performed by Wen *et al.* in a hydrogen-air obround detonation combustor, a second weak pressure spike was observed in the curved section which was absent in the linear section [35]. Pressure measurements using two transducers azimuthally spaced 45º apart in a fully annular RDC also detected the existence of trailing pressure spikes [36], further indicating the persistence of multi-shock structures in curved detonation channels. Recently, Mathews *et al.* used laser-absorption spectroscopy and detected the presence of a heat release zone trailing the leading detonation wave in the injection near field [37]. Batista *et al.* utilized large eddy simulations with up to 140 million cells to reveal the role of unsteadiness in the propagation of trailing waves and descending modal transition dynamics [28]. These and other simulations have identified the existence of reflected shocks and secondary or trailing detonations in annular configurations, which gives rise to the need for detailed experimental interrogation of the spatiotemporal distribution in representative annular geometries that have ample optical access and are amenable to numerical simulation. Several studies have been conducted with optically accessible RDCs for characterization of the detonation structure in annular channels [38–45]. Rankin *et al.* performed instantaneous high-speed chemiluminescence and infrared imaging in an optical non-premixed H_2-air RDC with radial-air and axial-fuel injection to observe the dependence of instantaneous and phase-averaged detonation wave structure on the mass flux and equivalence ratio [38]. On the same test platform, Fugger *et al.* increased the repetition rate of chemiluminescence imaging to 1 MHz for the same RDC and showed a highly non-uniform time-resolved curved detonation-front propagation [46]. Athmanathan *et al.* used 1 MHz broadband chemiluminescence and unsteady Reynolds averaged Navier-Stokes (URANS) simulations in a non-premixed H_2-air RDC with axial-air and radial-fuel injection, which revealed significant axial variations in the detonation wave structure within the reactant fill zone [41,47]. Similar observations were provided by Jodele et al., who showed an axial variation in the detonation structure with wake combustion fronts and transverse waves [48]. Recent OH* chemiluminescence measurements by Matsuoka *et al.* showed a luminous wave trailing the leading detonation front for test conditions with low injection pressure drop [49]. While these studies highlight the significant spatial inhomogeneities that can exist in RDCs, chemiluminescence imaging is inherently spatially averaged, and more detailed measurements are needed to investigate the coupling between the highly stratified reactant flowfield [50–53] and the complex detonation wave characteristics [50,54].

To provide further insight into the intricate spatiotemporal dynamics in curved detonation channels, the current work combines a recently developed MHz-rate OH PLIF capability [55] with simultaneous orthogonal imaging of MHz-rate chemiluminescence to capture the detailed 3D characteristics of the detonation wave structure in a non-premixed RDC. High-frequency surface mounted pressure measurements are also performed to complement the optical diagnostics. The experimental data are used to corroborate 3D URANS predictions of key detonation physics with the same RDC geometry and flow conditions, which in turn provides further information on the underlying physical phenomena and flow properties. The work is accomplished using an annular geometry designed for stable operation over a range of mass flow rates and with full optical access spanning from the air plenum to the exit plane [18]. The spatiotemporally resolved experimental data and corresponding 3D numerical simulations help to build greater understanding of the origin, nature, and implications of shock interactions with stratified reactants in annular RDC geometries.

2. Experimental Setup

2.1. Rotating detonation engine and instrumentation description

A schematic cross-section of the optically accessible RDC is shown in Figure 1 (a). A ~20 mm thick quartz outer body with an inner diameter of 136 mm serves as the outer wall for an annular detonation channel with a radial passage width of 10.7 mm. High-pressure air enters from a plenum through an annular converging-diverging section with a throat gap of 1.42 mm. Fuel is injected radially through 100 equally spaced slots in a jet-in-crossflow arrangement slightly downstream of the air injection throat. The fuel slots are milled with a 0.6 mm diameter end mill to a depth of 0.4 mm and are located at an area ratio (ε) of 1.16 relative to the area at the throat. The flow channel expands (at 10°) up to $\varepsilon = 1.81$, leading into the combustor channel ($\varepsilon = 7$) past a backward facing step (BFS) located 5 mm downstream of the fuel injection ring. The chamber length is ~95 mm from the fuel injection plane and ~ 90 mm from the BFS. The air and fuel injector stiffness $(P_{plenum} - P_{chamber})/P_{chamber}$ is ~2.2 for the current fuel injector configuration at a global equivalence ratio of ~1.0.

[Figure 1 about here]

An instrumented metal outer body constructed from SS316 is installed in place of the optical outer body for wall measurements of pressure and temperature, as shown in Figure 1 (b). Pressure transducers (UNIK 5000) and thermocouples (Omega K-type thermocouples) are used for monitoring the pressure and wall temperature and are sampled at 2 kHz with an uncertainty of ±1 psia and 0.1 K, respectively. Additionally, flush surface-mounted high-frequency pressure transducers (PCB 113B21) are installed to measure the instantaneous wall-pressure during detonation wave passage. The flush-mounted PCB transducers are aligned azimuthally and are axially spaced at ~14.5 mm (injection near field) and ~73.5 mm (injection far field) from the fuel injection plane. The PCB data are over-sampled at 5 MHz repetition rate using an HBM Genesis data acquisition system. A low-pass signal filter of 250 kHz is applied to the measured pressure in post processing to ensure measurements are well below the PCB resonant frequency of 500 kHz.

The hydrogen and air mass flows are metered using choked sonic nozzles. The dry air flow rate is varied from 0.21 kg/s to 0.9 kg/s to reach air throat mass fluxes of $G_{air} = 350$ kg/m^2/s to 1500 kg/m^2/s, respectively. Hydrogen is metered to reach a global equivalence ratio (ϕ_{global}) close to 1.0. The uncertainty in mass flow rates of both the fuel and air is computed to be ~2%.

2.2. 100 kHz and 1 MHz chemiluminescence imaging setup

The high-speed broadband chemiluminescence optical setup shown in Figure 2 (a) is employed at 100 kHz and 1 MHz repetition rates, with the former capturing multiple cycles for phase-averaged measurements and the latter capturing a single detonation wave passage per test due to limitations on frame count. For the 100 kHz imaging, a Vision Research Phantom v2012 is used to obtain ~10,000 frames with 300×300 pixels to capture ~400 detonation cycles occurring over 100 ms. This large image sequence dataset provides a statistically significant number of images to record the phase-averaged detonation wave structure at different operating conditions. The 1 MHz broadband chemiluminescence images are acquired using a Shimadzu HPV-X2 camera to collect 256 sequential frames with 250×400 pixels for time-resolved measurement of single detonation wave passages.

The high-speed cameras are coupled to an image intensifier (HiCatt 25, Lambert Instruments) capable of operating at speeds of up to 1 MHz. A 105 mm camera lens (UV-Nikkor, Nikon) with a minimum aperture of *f*/4.5 and a transmission spectrum ranging from UV to visible wavelengths is used with the imaging system. The intensifier time gate is set to 100 ns to allow sufficient signal while minimizing motion blur, giving a detonation wave displacement of less than 1 pixel during exposure. The camera is focused on the RDC annulus to visualize the axial-azimuthal (x-θ) structure of the wave traveling through a circumferential range of nearly 180º. The field of view (FOV) axially extends from ~5 mm upstream of the air-injection throat to ~15 mm upstream of the exit plane, as shown in Figure 2 (b). As the OH* chemiluminescence images are by nature line-of-sight integrated, it would not be possible to dewarp the images to account for the lensing effect of the quartz window without inducing false warping in the shape of the underlying flow structure. This is because locations near the inner diameter of the quartz would dewarp differently than the outer diameter. However, the spatial distortion induces a deviation on the order of 8–9% across the entire image in the azimuthal direction, which does not alter the field of view in a manner that would affect the interpretation of the results. Limit-cycle operation is achieved at ~20 ms after detonation wave initiation, with image acquisition starting at ~300 ms. The optical setup allows for imaging of broadband chemiluminescence with a spectral bandwidth of 280–800 nm, including OH* chemiluminescence (280–320 nm), emission from radicals in hydrogen-air combustion (320–500 nm), and visible to near-infrared emission from water vapor (>600 nm) [56]. The OH* chemiluminescence emission intensity is an order of magnitude higher than other species, as detailed in prior work [56].

[Figure 2 about here]

2.3. Simultaneous orthogonal MHz OH-PLIF and OH chemiluminescence imaging*

To understand the three-dimensional detonation wave structure, simultaneous/synchronized MHz-rate OH PLIF and MHz-rate OH* chemiluminescence measurements are performed in the radial-axial (r-x) and axial-azimuthal (x - θ) views, respectively, as shown in Figure 3 (a). The OH* chemiluminescence imaging system consists of a Shimadzu HPV-X2 camera coupled to a MHz-rate UV image intensifier (HS-IRO, LaVision) and a 45 mm UV lens (Cerco) with a minimum aperture of *f*/1.8. A UG11 spectral filter is used to limit the detected flame emission to OH*. The intensifier gate is set to 100 ns to limit blurring of the detonation wave motion to less than 1 pixel during image acquisition. Two silver UV-reflective mirrors (M1 and M2) are used to image the OH* chemiluminescence of the detonation wave in the axial-azimuthal (x-θ) FOV, which is orthogonal to the OH-PLIF laser-sheet entering at ~45° to vertical axis of the RDC, as shown in Figure 3(b). As the laser sheet for OH-PLIF is orthogonal to and spatially distinct from the OH* images, scattering from the OH-PLIF laser sheet on the RDC inner body provided a convenient marker (visualized as a line in the axial-azimuthal plane) to spatially relate the OH* images to the OH-PLIF excitation plane.

[Figure 3 about here]

The experimental setup used for the OH-PLIF measurements is described in the prior work by Hsu *et al.* [55] and is summarized here for convenience. An Nd:YAG burst-mode laser (Quasimodo, Spectral Energies, LLC) pumps an optical parametric oscillator (OPO) that is custom built (Spectral Energies, LLC) to produce a 4 ns wide, 284 nm excitation laser pulse at 1 MHz repetition rate to excite the $Q_1(9)$ transition of ground-state OH [55,57]. The pulse-train produces ~200 pulses at this repetition rate with ~400 μJ/pulse. The laser pulses are transmitted to the RDC test cell from a remote laser lab using UV-coated mirrors, and sheet-forming optics are used to form a ~0.5 mm thick × 100 mm wide laser sheet to visualize the radial-axial structure of the

detonation wave during passage. The laser sheet enters normal to the quartz cylinder and at an angle of 45º with the camera and the RDC vertical axis. Distortions through the curved quartz window can affect the images acquired by the OH-PLIF imaging system. For the radial-axial images presented in this study, the distortions in the axial-direction (x) are observed to be negligible. The object plane (PLIF plane) in this work, is positioned at a 45° angle to the camera, which can expect a compression effect of ~30% in the vertical direction of the object plane. However, the inner and outer curved surfaces of the curved quartz acts as a plano-concave lens, which stretches the object plane back by ~ 25%. Thus, the effect of the quartz window on the 45° angled placement of the laser-sheet and the imaging system serendipitously minimizes the expected optical distortion. The PLIF spatial domain provides an FOV extending axially from the fuel-injection site to the exit plane of the RDC, as shown in Figure 3 (b). A 320 ± 20 nm BPF (FF02-320/40-50, Semrock) is used to help spectrally separate the OH-PLIF signal from broadband flame emission and laser scattering. The resultant fluorescence is captured by a second Shimadzu HPV-X2 camera coupled to a second image intensifier (HiCatt 25, Lambert Instruments) and a UV 45 mm (*f*1.8) lens, with a time-gate of 40 ns to preferentially capture the OH-PLIF and temporally reject OH* chemiluminescence from the detonation front.

Both the MHz-rate OH* and OH-PLIF cameras are synchronized with the MHz burst-mode laser system and are remotely triggered by the RDC auto-sequence system at ~300 ms after initiation of detonation (several hundred wave passages after a steady detonation has been achieved).

2.4. Experimental procedure and conditions

The RDC test is remotely operated with automated valve and camera-trigger timing controlled by a 2 kHz data acquisition and control system (NI PXIe DAQ). At the start of the test, air and hydrogen are allowed to flow for ~0.5 seconds to prime the RDC with reactants. A H_2/O_2 predetonator charge enters radially outward into the primed combustion chamber at an axial location ~25 mm downstream of the fuel injection site. This charge initiates detonation waves that reach limit cycle behaviour within ~40 ms based on high-speed visualization of the end-view of the RDC, and the chemiluminescence and/or OH-PLIF imaging systems were triggered ~300 ms after RDC ignition. Each RDC test lasted for ~1 s after initiation, at the end of which the fuel valve was shut off and the fuel lines were purged with nitrogen.

Table 1: Operating Conditions of the RDC and camera settings of the diagnostics

Case	G_{air} ($kg/m^2/s$)	$\dot{m}_{air}$ (kg/s)	$\dot{m}_{hydrogen}$ (kg/s)	ϕ_{global}	Intensifier exposure			
					Broadband Chem.		Simultaneous 1-MHz OH-PLIF and OH* Chem.	
					100 kHz	1 MHz	PLIF	Chem.
1	350	0.21	0.007	1.1	100 ns	100 ns	-	-
2[1]	750	0.45	0.014	1.05	100 ns	100 ns	40 ns	100 ns
3	1125	0.68	0.021	1.07	100 ns	-	-	-

[1] Case 2 is considered the baseline condition for which various experimental data and URANS simulations are compared.

4	1500	0.91	0.029	1.06	100 ns	-	-	-

The operating conditions used in this study are tabulated in Table 1. The RDC is operated at four different mass fluxes, G_{air}, at a mean global equivalence ratio ϕ_{global} ~ 1.07 with a coefficient of variation of ~2% among the four cases. Because of the relatively small coefficient of variation in ϕ_{global}, the dominant parametric change across each case is assumed to be the change in the air-mass flux. Case 2 is considered the baseline condition for this study, where computational modelling was performed for comparison with the experimental results from broadband chemiluminescence and OH PLIF. Chemiluminescence imaging was performed at 100 kHz for all four cases and at 1 MHz for Cases 1 and 2. The high mass fluxes present in Cases 3 and 4 posed challenges associated with potential cracking of the quartz window due to high chamber pressures and heat flux loads. Hence, the MHz-rate experiments were not conducted for Cases 3 and 4 to avoid potential damage to the MHz-rate imaging equipment.

3. Numerical model

3.1. Model introduction and parameters

A complementary 3D URANS non-premixed simulation is performed using the experimental RDC geometry and flow conditions for the baseline Case 2. The URANS equations were solved with CFD++ developed by Metacomp [58], with the solver performance initially evaluated and qualified for compressible flow characterization in non-reacting supersonic environments [59]. For the reacting flow case of RDCs, a one-step chemistry model was implemented based on the reaction mechanism used by Frolov et al. assuming $2H_2 + O_2 \rightarrow 2H_2O$ with the hydrogen oxidation rates as $[\dot{H}_2] = -8\times10^{11} P^{-1.15}[H_2]^2[O_2]\ e^{10^4/T}$ *(atm, mol, L, s)* [60]. This approach has been utilized for capturing macro features such as detonation fronts, oblique shock waves, and contact surfaces in several investigations in both premixed [61,62] and non-premixed [63,64] rotating detonation configurations. Grid and time-step independence studies were performed on the reacting flow-solver in a two-dimensional detonation tube in prior work [34]. With a time-discretization of 0.1 μs and use of the one-step reaction model, the solver predicted a wave speed within 2% of the Chapman-Jouguet (C-J) condition. The results of the 3D URANS simulation were also compared with exhaust-gas temperatures available using coherent anti-Stokes Raman scattering thermometry in the same RDC geometry and showed reasonable agreement with statistical distributions [65].

[Figure 4 about here]

The numerical domain of the combustor, shown in Figure 4 (a), consisted of the air plenum, air injection throat, 100 fuel injection slots, and the combustion region downstream of the backward facing step (BFS). The numerical model encompasses the air plenum upstream up to 40 mm from the BFS. The individual fuel slots are modeled with a square cross section for ease of meshing, and aa length of 10 mm. A structured grid (ICEM CFD, ANSYS) with boundary layer mesh refinement was implemented with a total of ~48.5 million cells. The injection region and plenum downstream of the BFS have high mesh density to resolve the mixing region upstream of the detonation region, as indicated by the passage mesh shown in Figure 4 (a). Additionally, the first layer of the mesh on the inner end wall had a non-dimensional wall distance y+ value of less than 2 to resolve at least one point in the laminar sublayer. At locations within the detonation front, the maximum y+ of the first layer of the mesh was 14 and 2 on the outer and inner diameters of the annulus, respectively. A numerical hot-spot was generated to start the simulations. To speed up convergence, the simulations were initially started on a coarse grid (~4 million cells) for ~30 cycles

without resolving the boundary layer (slip walls). These results were then mapped on to a finer mesh until the converged limit cycle solution was achieved. Data presented in this work are obtained after ~30 cycles beyond the limit cycle solution. For the boundary-layer refined mesh, adiabatic non-slip walls were applied. The numerical boundary conditions were supplied from experimentally derived pressure measurements from test Case 2 (Table 1) with G_{air} = 750 kg/m^2/s and ϕ_{global} = 1.0. Boundary conditions included a total pressure of p_o = 5 bar and total temperature T_o = 290 K at the air plenum, a total pressure of p_o = 5.35 bar at the fuel injection ports, and a mixed supersonic/subsonic exit boundary condition with an outlet static pressure of p = 1 bar. The mass flow of the reactants converged to a steady state value of 0.02 kg/s for hydrogen and 0.62 kg/s for air. At steady state, the numerical model reached ϕ_{global} = 1.1. The CPU time to achieve one detonation cycle was approximately 48 hours on 120 high-performance computing (HPC) cores. Figure 4 (b) shows a pressure and temperature trace sampled every 5 μs for the last six detonation cycles at a radial location r = 59 mm near the inner wall of the annulus and an axial location of 1 mm downstream of the BFS. The high baseline temperatures above 1500 K in Figure 4 (b) show that this region is filled with exhaust gases expelled by the detonation wave and never quite reaches the fuel and air inlet temperatures. The implications of these residual exhaust gases in the recirculation region of the BFS will be discussed further below. The static pressure downstream of the recompression wave due to the detonation wave passage is ~4.8 bar.

In addition to the grid- and time-step independence trade-off studies performed for the solver, a commonly used parameter to compare simulation results with experiments is the percent deviation of detonation cycle frequency with the experimental counterpart. Prior work by Lietz *et al.* used a large eddy simulation (LES) model on a hexahedral grid with 90 million cells for a rotating detonation rocket engine (RDRE) and approached to within 8% of the experimental cycle frequency [26]. Sato et al. used a 28 million unstructured mesh in a non-premixed RDC and approached within 15% of the experimental cycle frequency with the same fuel-air combination in a comparable geometry [32]. In this work, the predicted RDC cycle frequency is within 7% of the experimental counterpart (4.3 kHz), with more detailed comparisons to the optical diagnostics discussed in the results to follow. Note that no adjustable simulation parameters were employed to artificially improve the comparisons with experimental results.

4. Results and discussion

The analysis of results is organized into three sections. Section 4.1 establishes the existence of a dual-wave system characterized by leading and trailing detonation waves that appear to be closely coupled by the local flow physics. This dual-wave system is persistent for all operating conditions listed in Table 1 and is consistent with prior pressure transducer traces and chemiluminescence images in other non-premixed annular RDCs [23, 33–37]. Section 4.2 provides a high-fidelity description of the detonation wave structure as a function of time throughout the entire RDC channel. This section shows the potential for unburned reactants in the injector near field to survive the leading detonation wave and to form a dual-wave detonation system due to mixing and shock-induced detonation of those reactants within the trailing azimuthal reflected shock system. While mixing dynamics are of general interest in non-premixed RDCs, the interaction of unburned reactants with azimuthal reflected shocks could explain why closely coupled dual-wave detonation structures have primarily been identified within annular geometries. Section 4.3 presents further details of the mixing dynamics to explain the underlying physical properties that lead to poor mixing and weak dual-wave detonation structures in the injector near field, in contrast with substantially more robust singe-wave detonations due to rapid mixing in the injector far field. This section also considers the impact of mixing-induced non-ideal detonation wave dynamics on the local pressure rise within non-premixed RDCs.

4.1. Description of the rotating detonation-wave structure and propagation

4.1.1. Broadband chemiluminescence measurements

MHz-rate broadband chemiluminescence images for Cases 1 and 2, corresponding to G_{air} = 350 kg/m^2/s and G_{air} = 750 kg/m^2/s, respectively, are analyzed to establish the overall detonation wave structure and propagation in the axial-azimuthal plane. While the chemiluminescence intensity is generally indicative of the number density of excited-state species, this can increase with temperature, pressure, and the rate of fuel consumption. As such, this section lays the foundation for the overall detonation wave dynamics across a range of conditions, with a more complete description of the underlying physics to be provided in the following sections.

The sample images in Figure 3 are cropped to show an FOV of ~83 mm × 83 mm, with the axial direction aligned with the reactant inflow and the azimuthal direction aligned with the direction of detonation wave propagation. The FOV extends from the fuel-injection plane to ~10 mm upstream of the RDC exit plane. A spatial transformation to map the curved azimuthal coordinate to a planar field was not employed since such transformations increase image blur in the vertical direction and reduce the spatial resolution. The camera aperture was reduced to ensure a large depth of field and allow the wave passage around the azimuthal direction to remain in focus for the entire FOV. The numbering sequence in each image in Figure 5 (a) and (b) represents the timestamp in microseconds (μs). The yellow line at 1 μs marks the BFS location, which is located ~5 mm axially downstream of the hydrogen injection site. Zone I and Zone II's axial length was determined a line plot of the signal along the (y-direction), where the axial location of 50% of the maximum signal was chosen to be the boundary between Zone I and II, an approach used for zone definitions in both Figure 5 and Figure 6.

Readily observable in Figure 5 is that the lower mass flux and lower axial fill rate for Case 1 lead to a detonation wave with a shorter axial extent as compared to a detonation wave (Label A) that spans the entire axial length of the FOV for Case 2. Both time sequences show a region of lower chemiluminescence intensity in the axial near field of the injector (Zone I) that precedes a region of higher intensity further downstream (Zone II). Although a causal relationship cannot be established from the chemiluminescence images alone, the lower intensity of Zone I in both cases correlates with the presence of a mixing zone closest to the fuel injector that limits the consumption rate of reactants, as well as low static properties due to the high injection velocities. The much longer axial extent of Zone I for the higher mass flux for Case 2 also correlates with lower residence times, an extended mixing zone, and lower static properties than for Case 1 in Figure 5 (a).

[Figure 5 about here]

Indirect evidence of limited reactant mixing in the near field is further supported by the existence of a trailing wave (Label B) that follows the leading detonation front at nearly the same speed throughout the time sequence. The appearance of a trailing wave with increased chemiluminescence signifies either heat release, a pressure rise, shock heating, or a combination of these phenomena leading to an increase in the number density of excited-state species. The MHz imaging data show definitively that the trailing waves are not features that are occurring from stochastic axial dynamics but rather are closely linked azimuthally to the leading detonation wave. Furthermore, the trailing wave is predominantly in the axial injection near field within Zone I, where unmixed

reactants are more likely to be present and more likely to be able to support a trailing detonation wave. The image sequence of over 50 μs is provided in the appendix for the baseline condition in Appendix Figure A.1. for the detailed wave passage behavior. Figure 6 shows phase-averaged images of the broadband chemiluminescence collected over multiple cycles with a 100 kHz framing rate for all four test conditions. Image-cross correlation and thresholding was used to select 100 visually similar images to obtain the phase-averaged image from the 10,000 image stack at each condition. As the flame luminosity increases from Cases 1 to 4, the camera intensifier gain settings were appropriately lowered to minimize overexposure of the imaging system. Hence, the intensity scales are normalized to the peak signal and only the relative spatial distributions of signals are of interest in this discussion.

Compared to the time-resolved data in Figure 3, the phase-averaged images appear spatially diffuse due to the cycle-to-cycle variations in the instantaneous detonation wave structure; however, a number of consistent features can be observed. The first is that the leading detonation wave (Label A in Fig. 3) shifts signficantly further downstream from Case 1 to 2, which is consistent with the effects of lower residence times and increased reactant stratification in the injection near field at the higher mass flux of Case 2. In addition, the distance from the leading wave to the trailing wave in the injector near field (Zone I) increases significantly from Case 1 to Case 2, which is consistent with reactant stratification increasing with mass flux due to the reduced residence time for mixing and reaction in the trailing wave. These trends continue at the higher mass flux of Case 3, but the phase-averagead images suggest that a rate limiting condition is being approached with increasing mass flux from Case 3 to 4. These features are all broadly in agreement with the effects of finite mixing rates in non-premixed RDCs, and the occurrence of trailing waves for all four conditions is in accord with the identification or trailing pressure spikes in curved detonation channels.

[Figure 6 about here]

As these features impact the combustion efficiency and pressure gain within the RDC, they have significant implications for optimizing performance. Because of the line-of-sight averaged nature of the chemilunescence images in Figure 5 and 6, however, a more complete 3D description of reactant stratification and the azimuthal shock structure in curved detonation channels [22,33,34] is sought in Section 4.2.

4.1.2. High-frequency pressure measurements

High-frequency pressure measurements from PCBs flush-mounted on the outer diameter of the detonaton channel are analyzed in this section for the baseline condition, Case 2, corresponding to G_{air} = 750 kg/m^2/s at ϕ_{global} = 1.05. PCB 1 and 2 are located at axial positions of ~14.5 mm and ~73.5 mm from the fuel injection plane to isolate the near-field and far-field presure traces. Time synchronous or phase-averaged pressure profiles from ~500 cycles are shown in Figure 7 to complement the phase-averaged detonation images shown previously in Figure 6.

The pressure profiles from PCB 1 and 2 indicate the presence of a leading steep fronted detonation wave both the near and far-field regions. However, PCB 1 in the near field shows a sudden drop in pressure beind the leading steep fronted wave, followed by another rise in pressure. The temporal separation between the pressure front and the trailing pressure front is ~12 μs, which corresponds to an azimuth separation of ~17 °. This closely matches the ~18 ° separation from the leading combustion front to the trailing wave as observed for Case 2 in the phase-averaged images. From the pressure trace of PCB 2 located in the far field,

however, the pressure is observed to monotonically decay after the passage of the leading detonation wave across the sensor, suggesting the absence of strong trailing pressure waves consistent with the far-field images Figure 6.

[Figure 7 about here]

4.2. Three-dimensional detonation wave structure and shock-flow interactions

4.2.1. Conceptualization of the radial-azimuthal detonation wave structure in non-premixed annular RDCs

Due to the curvature of the annulus in RDCs, the leading detonation wave forms an azimuthal reflected shock system to turn the burned gas in the wake of the detonation wave. For a ~10 mm channel with a mean diameter of ~100 mm, numerical and experimental studies have shown the existence of these trailing azimuthal shock systems in RDCs burning hydrogen and air [22,33,34]. In the current RDC, azimuthal shocks would also be expected to trail the leading wave in both Zones I and II, but as noted in Section 4.1 a trailing luminous wave is only observed in Zone I. This suggests the combustion of unburned reactants in Zone I. However, a key question remains regarding the nature of this luminosity and the 3D near-field shock structure.

In this subsection, the concept that will be referred to here as azimuthal reflected-shock combustion (ARSC) is discussed as a subset of the general phenomenon known as shock-induced combustion to lay the foundation for a more detailed analysis of the dual-wave detonation system identified in the prior sections. The ARSC concept is shown in a schematic representation of the radial-azimuthal plane in Figure 8. In the axial near field, hydrogen is injected through discrete fuel jets, which are surrounded by an air crossflow. While shear-induced mixing will occur around the fuel jet, causing partial premixing of reactants, the core of the jet is expected to have very high concentrations of hydrogen in the injection near field and the area between the jets is correspondingly expected to have very high concentrations of air. Hence, the main detonation wave, as shown, passes through the partially premixed region between the air stream and the hydrogen jets at the outer radius. Behind the detonation wave, a complex composition of product gas and unburned-vitiated reactants will then expand, and form reflected shocks so that the burned gas can turn to follow the curvature of the RDC. This wake shock structure is conceptually expected to increase the local temperature, increase mixing, and reduce the ignition delay of the unburned reactants that have passed the leading detonation wave. Eventually, these unburned vitiated reactants may combust, potentially behind one of the trailing shocks to give rise to an ARSC feature, as shown in Figure 5. The same reflected shock structure is also expected to occur within Zone II, but only if there are sufficient unburned reactants trailing the leading detonation wave. Note that the leading wave is not uniform in the radial direction, with the higher speed of sound in the hot recirculation zone near the BFS causing the detonation wave to have a convex leading front as shown in the schematic. This simple conceptual picture will be discussed in more detail below, focusing on the detonation wave structure as it propagates through the highly stratified reactants as well as through regions with varying levels of product recirculation.

[Figure 8 about here]

4.2.2. Radial-azimuthal detonation wave structure from URANS simulations of Case 2

Building on the concept of the ARSC, this section utilizes the URANS simulations to further elucidate the impact of mixing on the 3D detonation wave structure and propagation within Zones I and II. It moreover lays out the rationale for classifying the trailing

luminous wave as a secondary detonation front and discusses the impact of this dual-wave detonation system on the local pressure rise. Figure 9 (a) and (b) show contour plots of temperature, pressure, and radial velocity (v_{radial}) in the same radial-azimuthal plane as shown conceptually in Figure 8. The two sets of contour plots are selected to highlight key features of the detonation wave structure in Zones I and II at 15 mm and 40 mm, respectively, axially downstream of the fuel injection plane.

It is readily evident from Figure 9 (a) and (b) that relatively poor mixing in the injector near field leads to significant differences in the detonation fronts between Zones I and II, as well as in the distributions of post-detonation products. As the detonation front propagates through Zone I, it consumes partially premixed reactants around the highly stratified fuel jets, leading to an irregular flame front with lobes wrapping around each of those jets. In the post-detonation products, the unburned fuel and air exist in low temperature regions (Label A) that become stretched in a manner consistent with the expansion waves that are also evident in the pressure distribution (Label B). The data in Figure 9 (a) show that the unburned reactants in the post-detonation region of Zone I ultimately mix and burn in a secondary combustion wave well behind the leading detonation front. This results in a sudden increase in static temperature and pressure behind the curved dashed line (Label C) in the region marked ARSC in Figure 9 (a). It also results in an increase in total temperature from 2600 K to 3100 K and an increase in total pressure by 2×, as shown across Section A-A' in Figure 10. Correspondingly, the unburned hydrogen drops by over 80% across the ARSC front, and the spatial separation of the shock front to the combustion zone is less than 2 mm, indicating that the wave is pressure coupled [66,67]. That the curved dashed line (Label C) in Figure 9 (a) represents a shock front is confirmed by the sudden change in the velocity from radially outward to radially inward. In addition, the vitiated reactant gas is accelerated from an azimuthal velocity of ~600 m/s (induced by the leading detonation front) to ~900 m/s after the ARSC. Hence, it may be concluded that the pressure gain in Zone I is apparently bifurcated into a leading freely propagating detonation wave and a trailing shock-induced detonation wave.

[Figure 9 about here]

The observations of the radial-azimuthal detonation wave structure in Zone I from Figure 9 (a) are in sharp contrast to that shown in Figure 9 (b) for Zone II. Due to the additional time for mixing, the reactants are expected to be more well mixed than in Zone I. This results in the observed steep and relatively uniform detonation front aligned with the radial direction, and there is no evidence of stratified reactants in the detonation wave structure or the post-detonation products. In addition, a classical series azimuthal shock reflections (Label D) becomes apparent, as was also depicted in Figure 5. Upon close inspection, the reflection point of the curved shock (Label C) in Figure 9 (a) occurs at the same point along the inner radius of the RDC as the reflected shock in Figure 9 (b), helping to confirm the nature of the trailing combustion wave as shock-induced detonation. The trailing oblique shock system in Zone II (Label D) in Figure 9 (b) turns the flow of the product gas, similar to Zone I, but with no observable heat release. This suggests that the reactants are sufficiently well-mixed in Zone II to be mostly consumed at the leading detonation front with insufficient unburned reactants to support a trailing ARSC wave, consistent with the images of chemiluminescence in Figures 5 and 6. As the ARSC is a wake-shock feature that results from the detonation interaction with the curved walls and will not be present in linear channels, this may explain the detection of dual-wave and single-wave structures in the curved and linear sections, respectively, of obround geometries, in which both sections undergo similar reactant mixing characteristics. In cases where the mixing length may be relatively short, however, the unburned reactants may not be sufficient to support the ARSC. Nonetheless, there appears to be direct evidence of such trailing waves that can be retroactively identified in the literature [35–37,49]. For example, trailing waves with very similar characteristics are present in the videos posted in prior work using a similar geometry as utilized in here [49].

[Figure 10 about here]

4.2.3. Simultaneous MHz OH PLIF and OH* chemiluminescence compared with the URANS simulation

Thus far, we have provided experimental evidence for differences in the detonation wave structure and propagation due to the evolution of the mixing field from Zone I to Zone II, including the existence of a trailing luminous wave within Zone I. We have also introduced the concept of the ARSC and utilized URANS simulations to provide a plausible description of the detailed physics that lead to these differences. However, the line-of-sight averaged nature of the chemiluminescence images and lack of corresponding experimental data on the local temperature, pressure, and velocity fields prohibits direct verification that the observed experimental phenomena are evolving in the same detailed manner as the URANS predictions. In this section, results from simultaneous MHz OH PLIF and OH* chemiluminescence captured in orthogonal planes are used to provide unambiguous spatial distributions that can be compared directly with URANS simulations. Verifying the ability of URANS simulations to capture various features of the detonative wave structure and propagation provides more confidence in using the simulations to understand the underlying physics. Due to the one-step chemistry model, the URANS simulations are not used to directly compute the local non-equilibrium OH mole fractions, and as such the OH* chemiluminescence and OH-PLIF data are compared with temperature predictions. The OH* chemiluminescence signals capture regions with high levels of heat release, while ground-state OH detected by the PLIF system likewise mark regions with high-temperature products. This approach has been used in prior work to show close correspondence between dynamic flame structures [68], but it should be noted that the ground-state OH mole fraction can drop substantially (~50%) with only a slight drop in the peak temperature (~4%) [69]. For this reason, as well as additional effects of the local chemistry, the temperature does not scale linearly with the OH number density; however, regions with high levels of OH will have comparatively high temperatures.

[Figure 11 about here]

As shown previously in Figure 3, the OH-PLIF data were acquired in a radial-axial plane for the baseline condition of Case 2. The detonation wave azimuth positions marked by dashed lines in Figure 11 (a) correspond to the relative times at which the radial-axial OH-PLIF images were collected in Figure 11 (b). Similarly, the azimuthal positions marked by dashed lines in Figure 11 (c) correspond to the times at which the radial-axial temperatures slices were obtained from the URANS simulations in Figure 11 (d). Geometric scaling of 1:1 was maintained between the experimental OH-PLIF images and numerical temperature color maps. Differences in the detonation propagation speed of ~1640 m/s in the experiments and ~1800 m/s in the CFD, along with differences in chemical time scales due to the simplified chemistry in the URANS simulations, lead to variations in the azimuthal structure in the post-detonation region. Nonetheless, similar features can be observed in the evolution of the 3D detonation wave structure between the experimental and numerical data, as shown in Figure 11.

The regions bounded by the white dashed lines at 1 μs in Figure 11 (b) and (d) show the reactant penetration depth at that instant just prior to the arrival of the detonation wave. Regions labelled as OH near the BFS in Zone I and near the exhaust in Figure 8 (b) indicate the presence local high static temperatures, similar to the model prediction in Figure 11 (d) at 1 μs. Although the fresh incoming reactants are in contact with the high-temperature product gases, there is no observed contact surface deflagration as observed from the OH PLIF as well as the total temperature field, likely due to a combination of mixing and ignition delay times relative to the detonation cycle time of ~240 μs [70].

At 8 μs, the OH-PLIF image captures the spatial distribution of OH during the wave passage through the PLIF plane. The arrows marked at 8 μs show the progression of combustion as the wave passes through the PLIF plane and consumes the reactants. At 4 μs in the numerical model, a similar spatial distribution and progression of the high temperature fronts is observed in Zone I and II, suggesting that the numerical model captures key features of the detonation wave structure and progression. Furthermore, the OH-PLIF slices from 1–8 μs confirm the notional shape of the detonation front in Zone I, as shown previously in the inset of Figure 9 (a).

At 15 μs in Figure 11 (b), after the leading detonation wave passage, the entire channel is observed to be filled with OH, except for the injection near field in Zone I where there is a lack of lack of combustion within the pocket of non-premixed or partially premixed reactants. The numerical temperature distribution in Figure 11 (d) also shows the presence of a cold zone in the injection near field at 18 μs, suggesting that the leading front does not combust the unmixed cold reactants in the injection near field in Zone I. This unburned cold-gas pocket in the radial-azimuthal plane is denoted with Label A in Figure 9 (a).

At 19 μs, in Figure 11 (b), the unburned reactants in the injection near field of Zone I mix and eventually combust in the trailing azimuthal shock system, as shown previously in Figure 9 (a). Similarly, in the numerical temperature contours of Figure 11 (d), a sharp rise in temperature is observed at 27 μs in the injection near field of Zone I where cold reactants had previously persisted. Thus, the presence of an ARSC system behind the leading detonation wave suggests that the stratified reactant fields present in non-premixed RDCs can lead to dual heat release zone that are azimuthally spaced by the shock system.

To provide further experimental support for the observation that the trailing wave is indeed a detonation, the simultaneous chemiluminescence and PLIF images are examined in greater detail. The unburned reactants present in the wake of the detonation wave in Zone I are consumed near the outer wall within two frames from 17 μs to 18 μs (See Appendix Figure A.2). This time difference of 1 μs corresponds to an azimuthal spread of the trailing wave to be ~1.6 mm (from 1640 m/s × 1 μs), which is much smaller than commonly observed deflagrative wave front. Additionally, 2 MHz OH PLIF from a prior experiment at the baseline condition (not shown), indicates that the unburned reactants are consumed by ARSC within 2 frames (500 ns × 2 × 1640 m/s), providing further evidence that the ARSC flame front spans an azimuth distance of ~1.6 mm [55,57]. The numerical simulations also indicate that the shock and the heat-release coupling is less than 2 mm, which is characteristic of a detonation mode of combustion [66,67]. These observations indicate that non-premixed RDCs can have both types of detonation waves–freely propagating and shock-induced–in close succession, with each having a different impact on the local evolution of kinetic energy, heat release, and pressure rise. Hence, further thermodynamic analysis is required to compare the overall expected pressure gain and power extraction from ideal conditions of purely freely propagating versus mixed-mode detonations. A detailed orthogonal view of simultaneous OH* chemiluminescence and OH-PLIF image stack focusing on the detonation wave passing through the PLIF plane is provided in the appendix A.2.

4.3. Further insights from URANS simulations of the mixing field

The prior sections indicate that mixing and reactant stratification plays an important role in the propagation physics of non-premixed RDCs. In this section, data from the URANS simulations are used to interpret the reactant field ahead of the detonation wave to provide additional insights on the apparent sudden changes in the state of mixing and detonation wave dynamics from the near field (Zone I) to the far field (Zone II). The good qualitative agreement in the axial distribution of the simulation data with the

OH-PLIF and OH* chemiluminescence images provides confidence in exploring the mixing field that underlies the complex detonation structure in non-premixed systems.

An iso-view of local equivalence ratio (ϕ_{local}) contours ahead of the detonation wave at five different axial locations downstream of the injection plane is shown in Figure 12 (a), the radial-azimuthal spread at the five different axial locations is shown in Figure 12 (b) along with corresponding probability distribution functions (PDFs) in Figure 12 (c) for Case 2. An appropriate weighting function is applied to each numerical cell, prior to PDF determination, to minimize biasing effects from varying grid size. The lower and upper bounds of the equivalence ratio contours were set to 0.3 and 3, respectively, using detonability limits from Bykovskii [71] corresponding to cell sizes that are an order of magnitude higher than the combustor channel width [72,73]. In addition, two radial-axial planes are shown bounding five fuel injector sites and having a total azimuthal separation 18°. One of these radial-axial planes shows the local equivalence ratio contours, while the other shows the Mach number contours.
The primary phenomenon that leads to partial premixing is the turbulence induced shear-layer between the hydrogen jet and the airstream, leading to a local equivalence ratio between 0.5 and 2 at the periphery of the hydrogen jet core. This shear-layer mixing is perturbed by axial shocks present in the reactant jet flow path, which can alter the axial momentum and rate of diffusive mixing. The probability of the local equivalence ratio being below the detonability limit drops from 85% at 10 mm to 68% at 20 mm and 60% at 30 mm, while the probability of being above the limit drops from 9% at 10 mm to 6% at 20 mm and 4% at 30 mm. This indicates an increase in partial premixing and a greater chance of complete combustion in the axial direction, as might be expected. A much more drastic change in the PDFs is observed from the 30 mm to 40 mm axially downstream, where the reactant mixing improves rapidly and there is a much higher probability of finding reactants within the range of detonability. The sudden change in mixing at ~40 mm corresponds closely with the axial extent of the trailing detonation wave and the beginning of the very strong signals shown previously in the phase-averaged chemiluminescence image for Case 2 in Figure 6. Likewise, the PDF shape transitions from a bimodal distribution weighted at the equivalence ratio extremities in the injector near field to a more uniform spread through the entire range of equivalence ratios that support stable detonation wave. This step increase in mixing can be attributed to the sudden drop in local Mach number from supersonic to subsonic, which greatly increases the residence time and promotes mixing of the reactants. Additionally, the slower reactant jet also expands radially, filling the entire channel width, providing further volume for turbulent and diffusive mixing. Trend continues at 50 mm, where the globally fuel rich test condition weights the distribution towards fuel rich equivalence ratios. These data provide confidence in the description of the two axial Zones I and II. Zone I contains mostly unmixed, very fast-moving fluid with low static quantities, and is limited to a radial fill of 4–5 mm from the outer diameter of the annulus. Zone II contains relatively well-mixed reactants and slow-moving fluid with higher static quantities that fill the entire 10.7 mm radial depth of the annulus.

[Figure 12 about here]

The predicted Mach numbers from the URANS simulations also help to explain the changes in the detonation axial wave height seen previously in Figure 6, which shows an increase in axial wave height for increasing mass flux from Case 1 to 2 but appears to reach a rate limiting condition with increasing mass flux up to Case 4. The high-speed reactants ahead of the detonation wave can be interpreted as an analogous supersonic free jet entering the expanding annular channel. Prior experiments on supersonic free jets have shown that the centreline velocity decay constant remains the same for Reynolds numbers varying by two orders of magnitude (~10^5 to 10^7) [36,37]. Consequently, while the supersonic core of the jet increases in length, the penetration depth of the supersonic/subsonic jet starts to show a plateauing behavior with increasing jet mass flux. In this RDC, the Reynolds

number of the supersonic reactant jet is estimated (from URANS and momentum balance) to vary between 1×10^6 and 6×10^6 from Cases 2 to 4. This is within the Reynolds number bounds of the aforementioned experimental results such that the reactant total penetration depth and the wave height starts to stabilize despite the increasing axial momentum. For this reason, the overall detonation wave height and the corresponding spatial extent and mixing fields in Zone I and Zone II also appear to reach a limiting condition from Cases 2 to 4.

The implication of such zone bifurcations is extremely important in designing non-premixed RDCs. The formation of shock induced detonations in the wake of the leading wave provides an avenue for the vitiated unburned reactants to burn in an isochoric fashion. While this isochoric vitiated heat release is desirable from a thermodynamic standpoint, where the injected reactants are burned before being expelled out of the RDC, there is a drop in the local pressure gain compared with that which is expected from freely propagating detonative combustion. For nearly stoichiometric, well-mixed hydrogen-air quiescent reactants, the total pressure ratio across a freely propagating detonation wave is expected to be ~15. In Zone I, from the URANS simulation results, the pressure ratio across the leading front is only ~ 4.5, in contrast with the leading front in Zone II where the pressure ratio of ~12 is much closer to the theoretical value. The pressure ratio in the ARSC at 1.8 is much lower than the leading front due to the reactant having an azimuthal approach velocity induced by the leading detonation wave in Zone I, which is a departure from freely propagating C-J detonations. Combining the 1.8 pressure ratio across the trailing ARSC, the total pressure ratio across the Zone I mixed-mode detonation (weak leading front and trailing ARSC) amounts to ~8.1. Due to the relatively simple reaction mechanism in the current URANS model, more accurate predictions of the absolute thermodynamic losses associated with mixed-mode detonation are needed; nonetheless, the current model predictions highlight the influence of the mixing field on the detonation wave structure and the potentially stark differences in the pressure gain that may result in partially premixed and well-mixed regions of non-premixed RDCs.

5. Conclusion

Simultaneous MHz-rate chemiluminescence and OH-PLIF imaging was performed to spatiotemporally resolve secondary detonation wave behavior and wall curvature effects in non-premixed rotating detonation combustors. Complementary three-dimensional (3D) URANS simulations of the same geometry and inflow conditions are also evaluated and are in overall good agreement with the experimental data. The combined experimental and numerical data provide detailed insight into the coupled effects of inflow conditions, reactant stratification, and shock-flow interactions on the structure and propagation of dual-wave detonation systems, as listed below:

- *Axial distribution of the detonation wave structure.* In non-premixed axial-flow RDCs, supersonic injection of reactants leads to a zone consisting of highly stratified reactants and a bifurcated dual-wave detonation system in the injector near field (Zone I). After a sudden drop to subsonic conditions, rapid mixing supports a stronger, single-wave detonation structure in the injector far field (Zone II). The transition from Zone I to Zone II, which depends on the local fluid properties, geometry, and mixing rates, is well predicted by the numerical simulations.
- *Origins of the azimuthally bifurcated detonation wave in Zone I.* The bifurcated detonation wave structure in the axial near field of the injector (Zone I) originates from the incomplete combustion of the highly stratified reactants that are outside the detonation limits of hydrogen and air. The azimuthal separation between the leading and trailing

bifurcated waves is overpredicted by the numerical simulations, likely due to the simplified chemistry of the simulations and/or the difficulty in capturing the shock-flow interactions.

- *The azimuthal reflected-shock combustion (ARSC) region.* The unburned reactants in the wake of the leading detonation wave undergo rapid mixing and subsequent reaction in a wall-curvature induced ARSC region within annular detonation channels. The trailing wave is identified as a shock-induced detonation from the increase in temperature, pressure, and velocity, as well as the measured detonation wave evolution from the 1 MHz OH PLIF images and high-speed pressure transducer measurements.
- *Local pressure rise due to dual-wave detonation systems.* Due to the aforementioned dynamics in the injection near field, there exists a leading freely propagating detonation wave followed by a shock induced detonation wave in the wake, with the combined heat release process of this dual-wave system having a lower pressure rise compared to the single freely propagating detonation wave in the well-mixed zone downstream (Zone II).
- *Mixing with detonation products.* Other features that are specific to each combustor include the presence of recirculation zones and the level of reactant vitiation and deflagration. The presence of recirculation zones in the injector near field of the current RDC, which has also been identified in prior studies, appears to alter the shape of leading detonation wave by establishing a vitiated mixture of fresh reactants and hot products from the previous detonation cycle ahead of the detonation wave. The vitiation of reactants in contact with the hot products near the exit of the combustor also alter the shape of the detonation front.
- *On the utility of the laser-based diagnostics.* Because of the inability to distinguish recirculation zones through line-of-sight averaged images of chemiluminescence, it has been difficult to surmise their precise role in the detonation wave dynamics. Hence, the simultaneous OH-PLIF and chemiluminescence imaging was critical in understanding the precise three-dimensional nature of the detonation wave structure and propagation through these zones and through the stratified reactants.

The complementary experimental measurements and 3D URANS simulations offer a deeper understanding of the observed secondary detonation wave phenomena. While each RDC will have differences in the injection configurations, mixing rates, and flow properties, it may be broadly concluded that the interaction of the detonation wave with the stratified reactants as well as interaction of the stratified reactants with shock reflections from curved chamber walls are important considerations for analyzing the wave stability and combustion efficiency in non-premixed RDCs.

Acknowledgments.

The authors would like to thank Dr. Paul Hsu and Dr. Naibo Jiang from Spectral Energies, LLC for assistance with the development of MHz-rate OH PLIF. The authors would also like to thank Christopher Crabtree, Bebe Wang and Dr. Jordan Fisher for experimental assistance. Funding for equipment was provided, in part, under AFOSR Award No. FA9550-16-1-0315 (Dr. Martin Schmidt, Program Officer) and DTRA Award No. HDTRA1-17-1-0031 (Dr. Jeffery Davis, Program Manager).

Appendix:

A.1: MHz rate OH* Chemiluminescence image sequence of detonation wave passage at the baseline condition (Case 2).

[Figure A.1 about here]

A.2: Simultaneous MHz rate orthogonal views of radial-axial OH PLIF and axial-azimuthal OH* chemiluminescence image sequence of detonation wave passing through the PLIF plane at the baseline condition

[Figure A.2 about here]

Figures:

List of Figures:

Figure	Caption
1	Figure 1: (a) Schematic of the radial-axial (r-x) cross-section of the flow path with the optical quartz body installed. (b) Instrumented outer body (SS316) indicating the axial position of flush-mounted PCB installation locations referenced to the fuel injection axial location.
2	Figure 2: (a) Optical setup for broadband/OH* chemiluminescence at 100 kHz and 1 MHz repetition rate showing the axial (x), azimuthal (θ), and radial (r) coordinate system. (b) Broadband chemiluminescence field of view (FOV) along the axial-azimuthal (x-θ) plane.
3	Figure 3: (a) Experimental setup of simultaneous orthogonal MHz PLIF and OH* chemiluminescence. A bandpass filter F1 is used to isolate the OH-PLIF signal (FF02-320/40-50, Semrock) and F2 for the OH* chemiluminescence signal (UG11, Schott) in the radial-axial (r-x) and axial-azimuthal (x-θ) planes, respectively. Silver mirrors (M1 and M2) are used to route the OH* chemiluminescence signal along an orthogonal path with respect to the OH-PLIF plane. (b) Details of the orthogonal OH-PLIF (r-x) and OH* chemiluminescence (x-θ) FOVs.
4	Figure 4: (a) Computational domain and mesh refinement, and (b) pressure and temperature traces 1 mm downstream of the backward facing step (BFS) [65].
5	Figure 5: MHz broadband chemiluminescence image sequence of detonation wave propagation for (a) Case 1 and (b) Case 2 (baseline condition). Each sequence was normalized to its own peak value because the camera intensifier gain was increased substantially for Case 1 to optimize the signal-to-noise ratio. Sequential numbering corresponds to 1 μs time steps. Zones I and II show regions with weaker and stronger chemiluminescence, respectively. A persistent trailing combustion wave is marked at 9 μs for both Cases 1 and 2, labelled as B and C, respectively.
6	Figure 6: Phase-averaged images of detonation wave for the four different mass flux cases investigated in this study. The dashed white lines show the presence of trailing luminous waves in the injection near field. Approximate scale markers for Zones I and II are added for spatial reference.
7	Figure 7: Time-synchronous phase-averaged pressure profiles from the high-frequency flush mounted PCBs in the injection near field and far field for the baseline test Case 2.
8	Figure 8: Schematic representation of the detonation wave structure in the radial-azimuthal plane and origin of the ARSC within Zone I.
9	Figure 9: URANS radial-azimuthal plots of static temperature, static pressure, and radial velocity at (a) 15 mm and (b) 40 mm axially downstream of the injection plane (in Zones I and II, respectively). A – Unburned reactants that survive the primary detonation wave, B – shock formation due to interaction of detonation product gas and cold hydrogen jets, C – shock front that induces the azimuthal reflected-shock combustion (ARSC), D – azimuthal shocks that turn the product gas in the annular channel. Profiles across A-A' are

	plotted in Figure 10.
10	Figure 10: Profiles of total pressure, total temperature, and azimuthal velocity across Section A-A' in Figure 9 (a).
11	Figure 11: (a) Axial-azimuthal (x- θ) and (b) radial axial (r-x) views of simultaneous OH* chemiluminescence and OH PLIF, respectively. (c) Axial-azimuthal (x- θ) and (d) radial axial (r-x) views URANS total temperature during the detonation wave passage in the. The axial-azimuthal views and the radial-axial views of experiments and simulations are scaled 1:1. See Appendix A.2 for sequential time-resolved simultaneous OH* chemiluminescence and OH-PLIF images.
12	Figure 12: Evolution of mixing characteristics from the injection site (a) radial/azimuthal equivalence ratio contours at five equally spaced axial locations ahead of the detonation wave. Two radial axial slices are presented 15° apart azimuthally, showing the local equivalence ratio and the Mach number at the hydrogen site. (b) Radial-azimuthal local equivalence ratio contour ahead of the detonation, indicating the fuel-oxidizer mixing at 5 axial locations spaced from the fuel-injection plane (c) Normalized weighted distribution of local equivalence ratio showing the transition from an unmixed (bimodal) distribution to a well-mixed distribution with increasing axial separation of the wave from BFS.
A.1	Figure A.1: OH* Chemiluminescence showing the detonation evolution at 1 MHz repetition rate at the baseline condition (Case 2). Consecutively numbered images were captured with a time-step of 1 μs and an image exposure of 100 ns.
A.2	Figure A.2: Image sequence showing orthogonal views of the radial-axial OH-PLIF plane and axial-azimuthal OH* chemiluminescence plane revealing the internal structure of the detonation wave as well as presence the trailing azimuthal reflected shock combustion feature (ARSC). The PLIF-sheet is visible as a line in the OH* chemiluminescence images from the phosphorescence of the quartz-outerbody. The detonation in this dataset is in the opposite direction as that in Figure A.1 due to the stochastic nature of the initiation process.

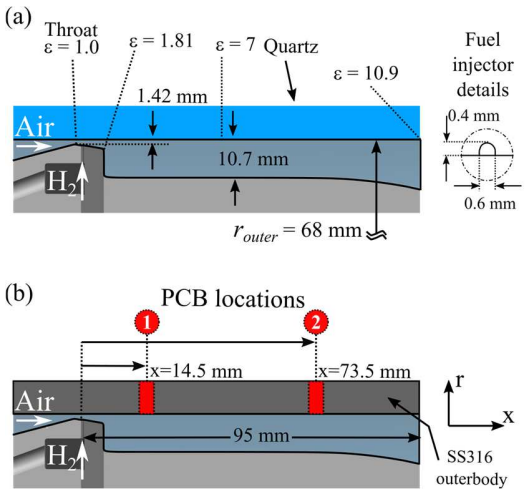

Figure 1: (a) Schematic of the radial-axial (r-x) cross-section of the flow path with the optical quartz body installed. (b) Instrumented outer body (SS316) indicating the axial position of flush-mounted PCB installation locations referenced to the fuel injection axial location.

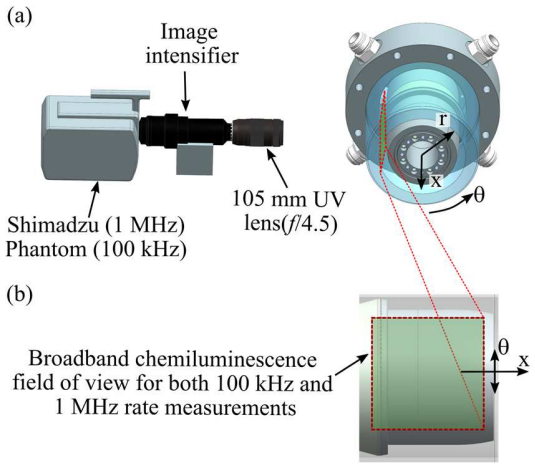

Figure 2: (a) Optical setup for broadband/OH* chemiluminescence at 100 kHz and 1 MHz repetition rate showing the axial (x), azimuthal (θ), and radial (r) coordinate system. (b) Broadband chemiluminescence field of view (FOV) along the axial-azimuthal (x-θ) plane.

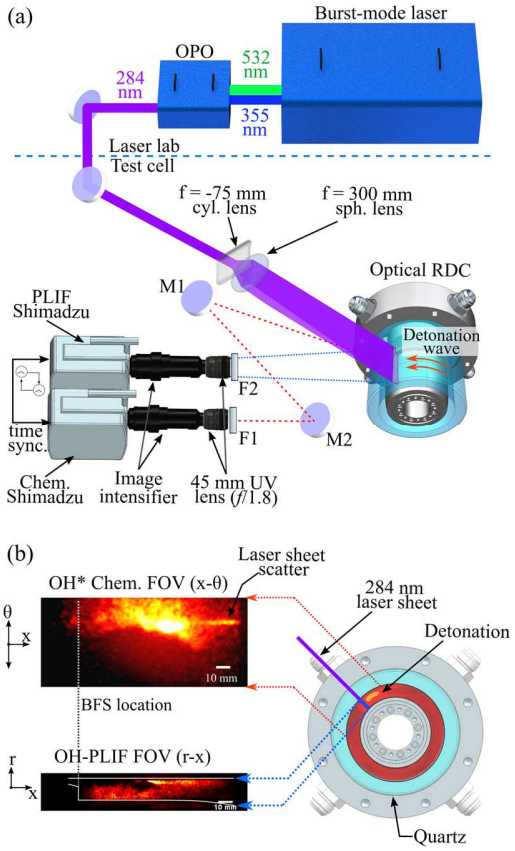

Figure 4: (a) Experimental setup of simultaneous orthogonal MHz PLIF and OH* chemiluminescence. A bandpass filter F1 is used to isolate the OH-PLIF signal (FF02-320/40-50, Semrock) and F2 for the OH* chemiluminescence signal (UG11, Schott) in the radial-axial (r-x) and axial-azimuthal (x-θ) planes, respectively. Silver mirrors (M1 and M2) are used to route the OH* chemiluminescence signal along an orthogonal path with respect to the OH-PLIF plane. (b) Details of the orthogonal OH-PLIF (r-x) and OH* chemiluminescence (x-θ) FOVs.

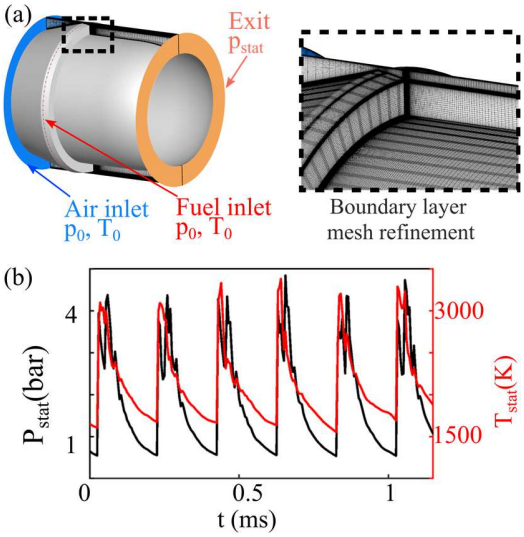

Figure 3: (a) Computational domain and mesh refinement, and (b) pressure and temperature traces 1 mm downstream of the backward facing step (BFS) [65].

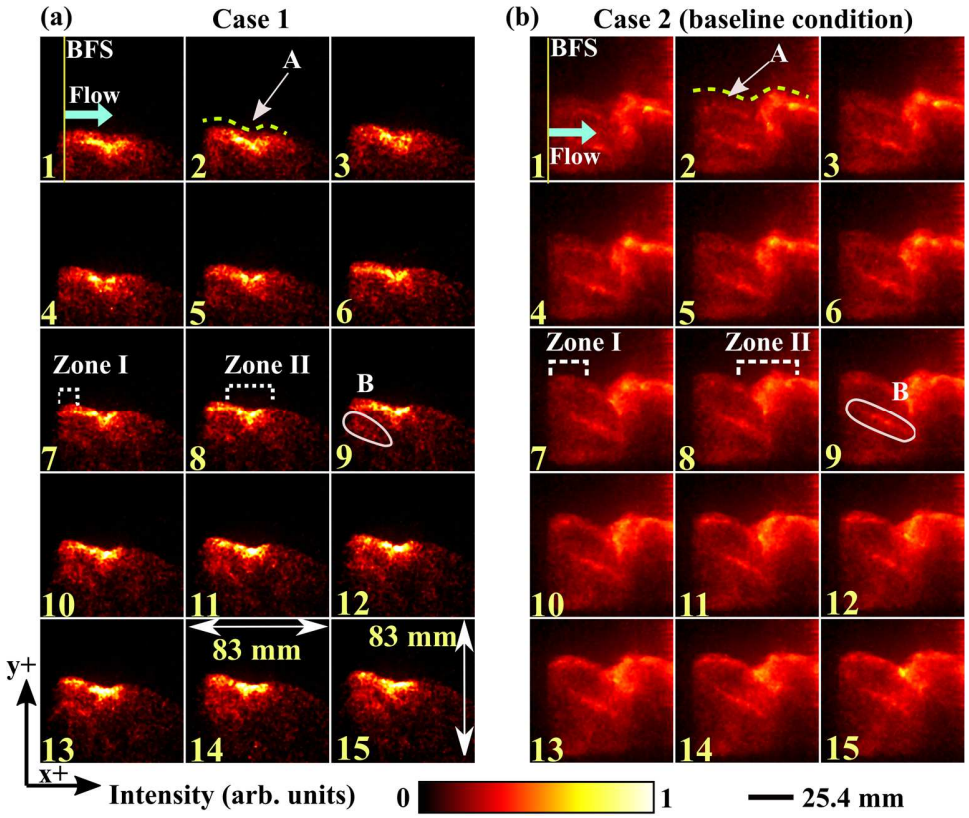

Figure 5: MHz broadband chemiluminescence image sequence of detonation wave propagation for (a) Case 1 and (b) Case 2 (baseline condition). Each sequence was normalized to its own peak value because the camera intensifier gain was increased substantially for Case 1 to optimize the signal-to-noise ratio. Sequential numbering corresponds to 1 µs time steps. Zones I and II show regions with weaker and stronger chemiluminescence, respectively. A persistent trailing combustion wave is marked at 9 µs for both Cases 1 and 2, labelled as B and C, respectively.

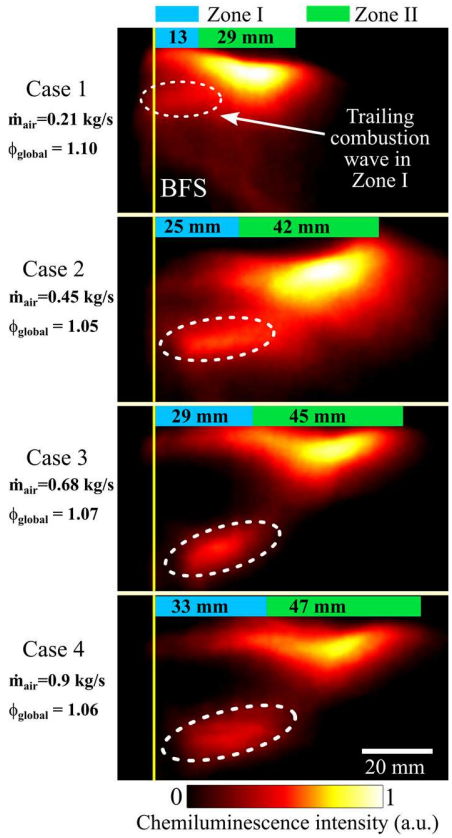

Figure 6: Phase-averaged images of detonation wave for the four different mass flux cases investigated in this study. The dashed white lines show the presence of trailing luminous waves in the injection near field. Approximate scale markers for Zones I and II are added for spatial reference.

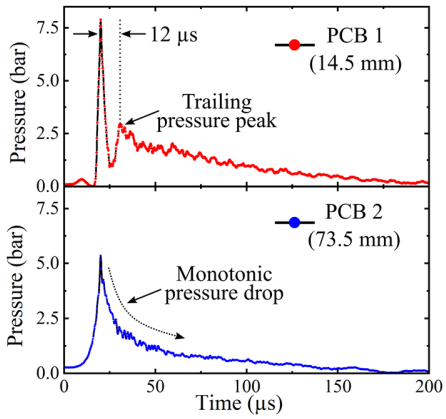

Figure 7: Time-synchronous phase-averaged pressure profiles from the high-frequency flush mounted PCBs in the injection near field and far field for the baseline test Case 2.

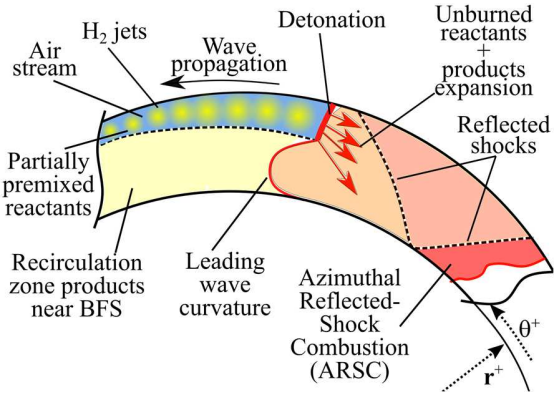

Figure 8: Schematic representation of the detonation wave structure in the radial-azimuthal plane and origin of the ARSC within Zone I.

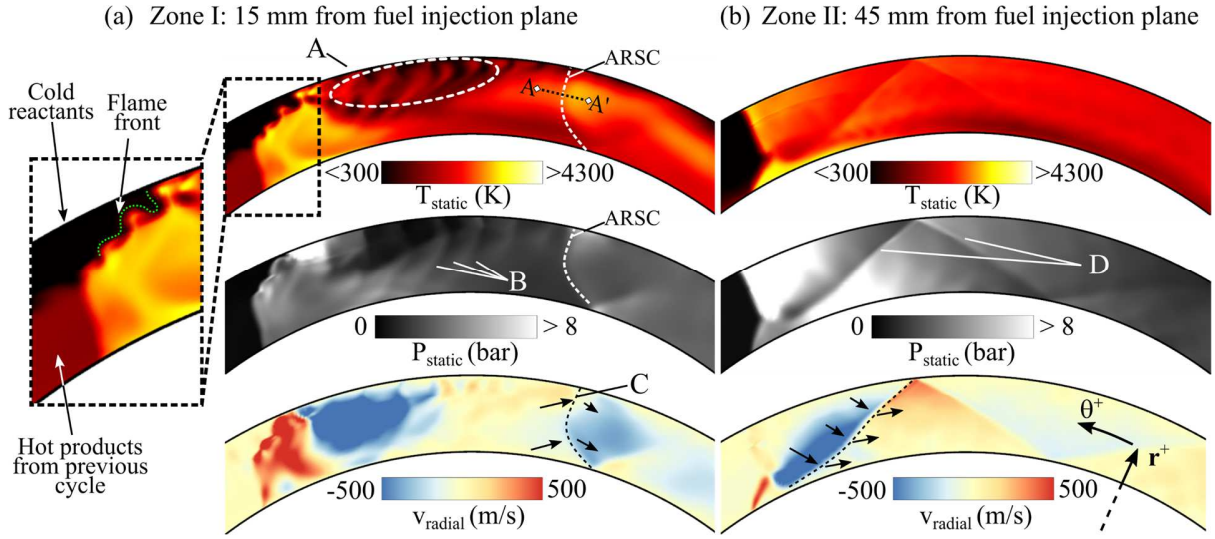

Figure 9: URANS radial-azimuthal plots of static temperature, static pressure, and radial velocity at (a) 15 mm and (b) 40 mm axially downstream of the injection plane (in Zones I and II, respectively). A – Unburned reactants that survive the primary detonation wave, B – shock formation due to interaction of detonation product gas and cold hydrogen jets, C – shock front that induces the azimuthal reflected-shock combustion (ARSC), D – azimuthal shocks that turn the product gas in the annular channel. Profiles across A-A' are plotted in Figure 10.

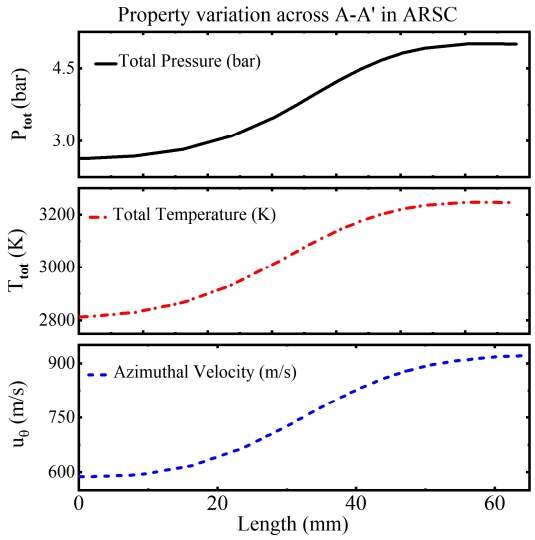

Figure 10: Profiles of total pressure, total temperature, and azimuthal velocity across Section A-A' in Figure 9 (a).

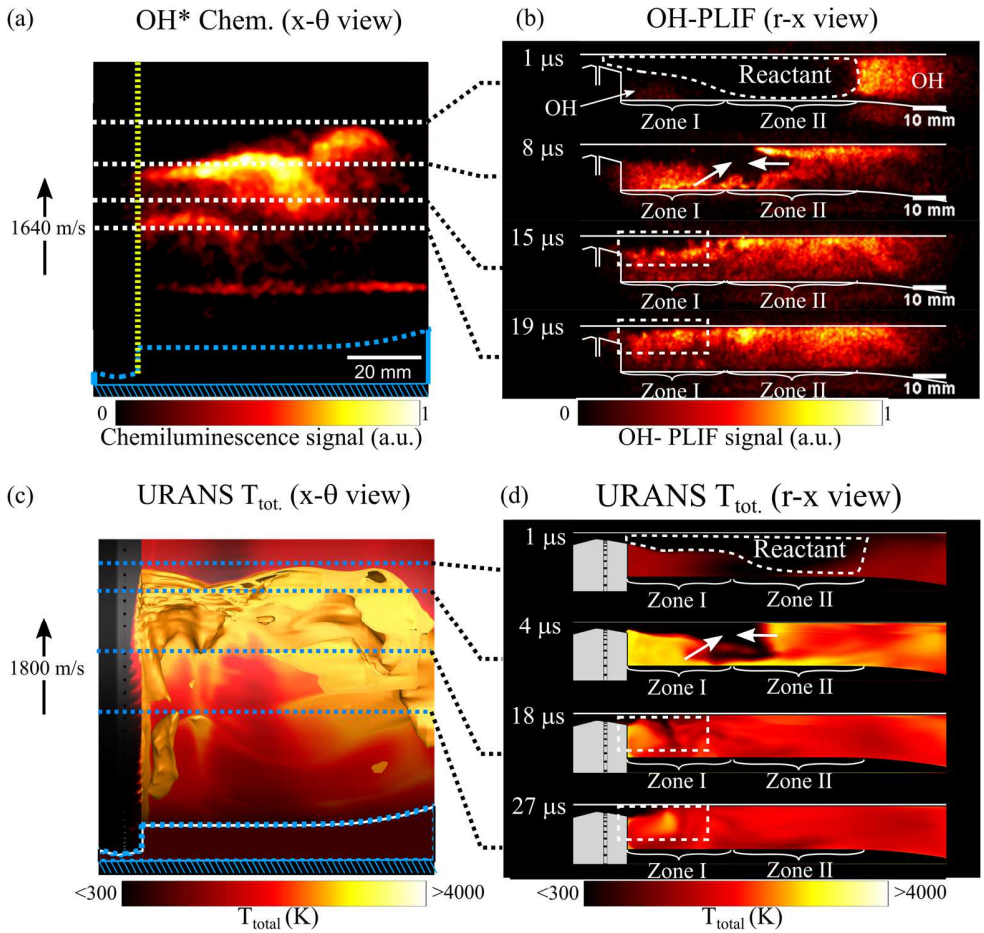

Figure 11: (a) Axial-azimuthal (x-θ) and (b) radial axial (r-x) views of simultaneous OH* chemiluminescence and OH PLIF, respectively. (c) Axial-azimuthal (x-θ) and (d) radial axial (r-x) views URANS total temperature during the detonation wave passage in the. The axial-azimuthal views and the radial-axial views of experiments and simulations are scaled 1:1. See Appendix A.2 for sequential time-resolved simultaneous OH* chemiluminescence and OH-PLIF images.

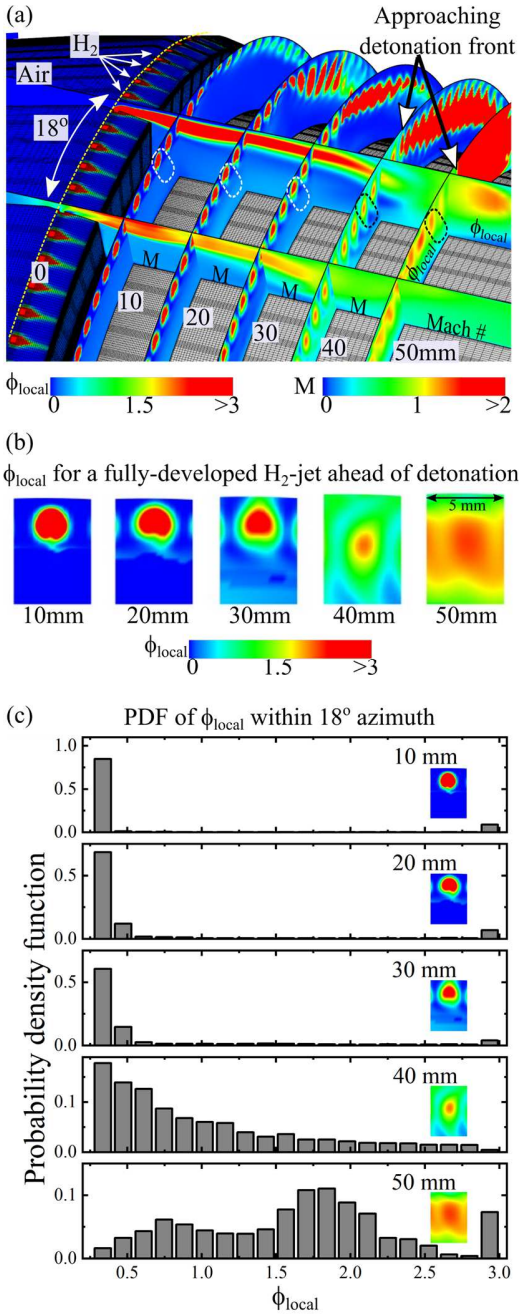

Figure 12: Evolution of mixing characteristics from the injection site (a) radial/azimuthal equivalence ratio contours at five equally spaced axial locations ahead of the detonation wave. Two radial axial slices are presented 15° apart azimuthally, showing the local equivalence ratio and the Mach number at the hydrogen site. (b) Radial-azimuthal local equivalence ratio contour ahead of the detonation, indicating the fuel-oxidizer mixing at 5 axial locations spaced from the fuel-injection plane (c) Normalized weighted distribution of local equivalence ratio showing the transition from an unmixed (bimodal) distribution to a well-mixed distribution with increasing axial separation of the wave from BFS.

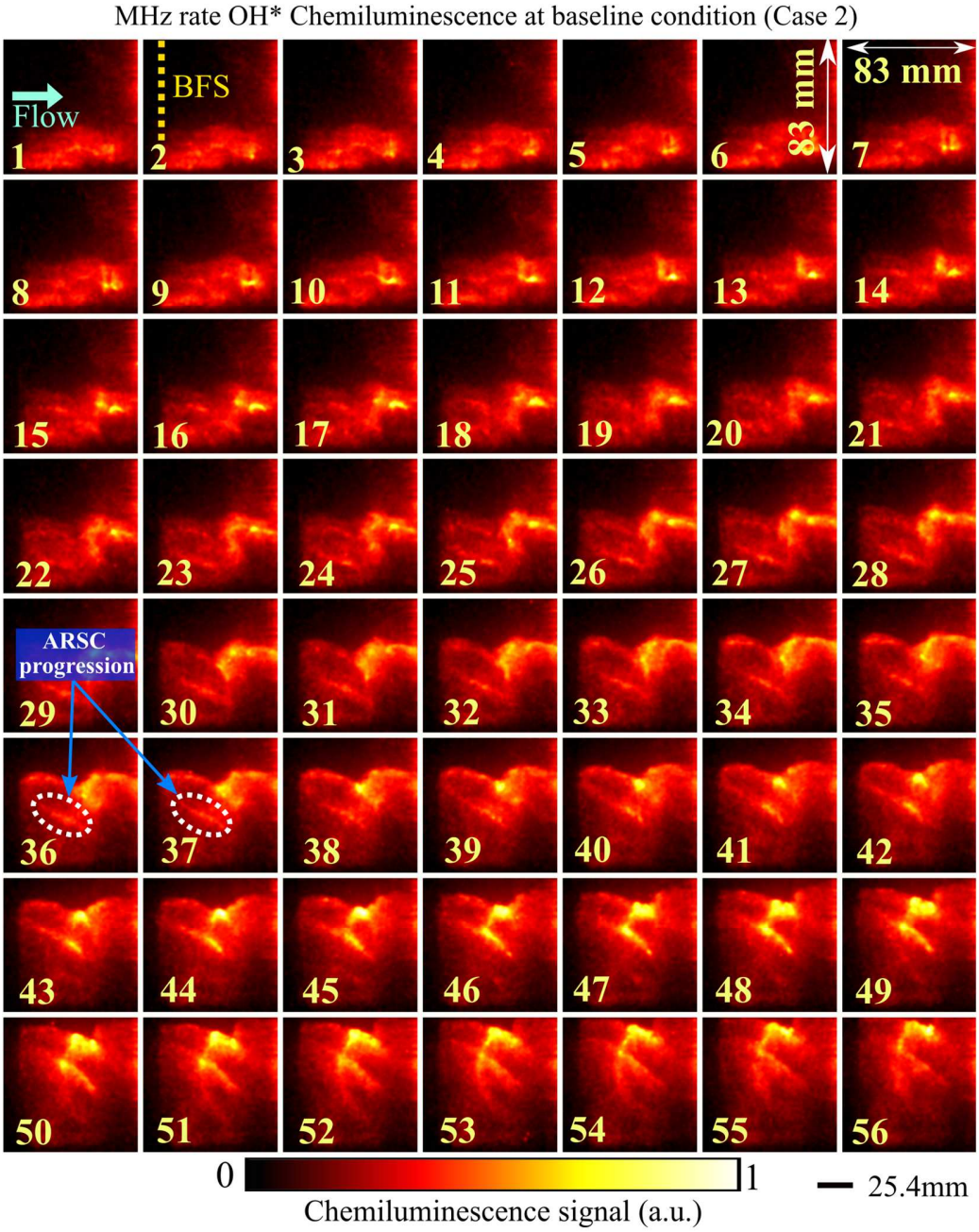

Figure A.1: OH* Chemiluminescence showing the detonation evolution at 1 MHz repetition rate at the baseline condition (Case 2). Consecutively numbered images were captured with a time-step of 1 μs and an image exposure of 100 ns.

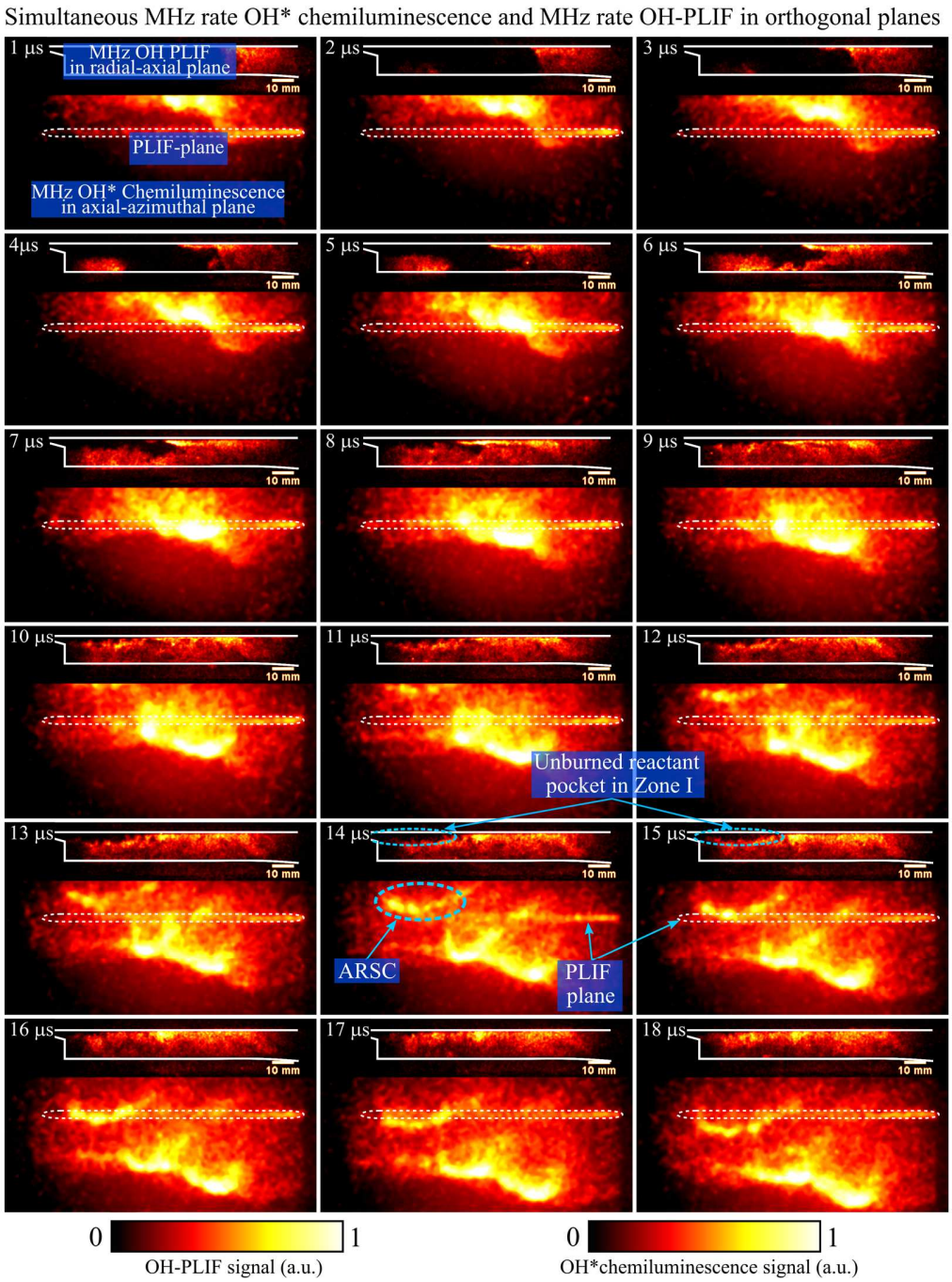

Figure A.2: Image sequence showing orthogonal views of the radial-axial OH-PLIF plane and axial-azimuthal OH* chemiluminescence plane revealing the internal structure of the detonation wave as well as presence the trailing azimuthal reflected shock combustion feature (ARSC). The PLIF-sheet is visible as a line in the OH* chemiluminescence images from the phosphorescence of the quartz-outerbody. The detonation in this dataset is in the opposite direction as that in Figure A.1 due to the stochastic nature of the initiation process.

References

[1] C.A. Nordeen, D. Schwer, F. Schauer, J. Hoke, T. Barber, B. Cetegen, Thermodynamic model of a rotating detonation engine, Combust. Explo. Shock 50 (2014) 568–577.

[2] V. Anand, E. Gutmark, Rotating detonation combustors and their similarities to rocket instabilities, Prog. Energ. Combust. 73 (2019) 182–234.

[3] P. Wolański, Detonative propulsion, P. Combust. Inst. 34 (2013) 125–158.

[4] J.Z. Ma, M. Luan, Z. Xia, J. Wang, S. Zhang, S. Yao, B. Wang, Recent Progress, Development Trends, and Consideration of Continuous Detonation Engines, AIAA J. 58 (2020) 1–59.

[5] M. Zhao, M.J. Cleary, H. Zhang, Combustion mode and wave multiplicity in rotating detonative combustion with separate reactant injection, Combust. Flame 225 (2021) 291–304.

[6] F.A. Bykovskii, S.A. Zhdan, E.F. Vedernikov, Continuous spin detonation of hydrogen-oxygen mixtures. 2. Combustor with an expanding annular channel, Combust. Explos. Shock Waves 44 (2008) 330–342.

[7] F.A. Bykovskii, S.A. Zhdan, E.F. Vedernikov, Continuous spin detonation in annular combustors, Combust. Explo. Shock 41 (2005) 449–459.

[8] K. Kailasanath, Review of propulsion applications of detonation waves, AIAA J. 38 (2000) 1698–1708.

[9] F. K. Lu, E. M. Braun, Rotating Detonation Wave Propulsion: Experimental Challenges, Modeling, and Engine Concepts, J. Propul. Power 30 (2014) 1125–1142.

[10] C. Welch, D. Depperschmidt, R. Miller, J. Tobias, M. Uddi, A.K. Agrawal, S. Lowe, Experimental Analysis of Wave Propagation in a Methane-Fueled Rotating Detonation Combustor, Proceedings of the ASME Turbo Expo 2018: Turbomachinery Technical Conference and Exposition 4B (2018), paper GT2018-77258.

[11] R. Bluemner, M.D. Bohon, C.O. Paschereit, E.J. Gutmark, Effect of inlet and outlet boundary conditions on rotating detonation combustion, Combust. Flame 216 (2020) 300–315.

[12] E. Bach, P. Stathopoulos, C.O. Paschereit, M.D. Bohon, Performance analysis of a rotating detonation combustor based on stagnation pressure measurements, Combust. Flame 217 (2020) 21–36.

[13] J.R. Burr, K.H. Yu, Experimental characterization of RDE combustor flowfield using linear channel, P.

Combust. Inst. 37 (2019) 3471–3478.

[14] K. Schwinn, R. Gejji, B. Kan, S. Sardeshmukh, S. Heister, C.D. Slabaugh, Self-sustained, high-frequency detonation wave generation in a semi-bounded channel, Combust. Flame 193 (2018) 384–396.

[15] C.L. Journell, R.M. Gejji, I. V. Walters, A.I. Lemcherfi, C.D. Slabaugh, J.B. Stout, High-Speed Diagnostics in a Natural Gas–Air Rotating Detonation Engine, J. Propul. Power 36 (2020) 498–507.

[16] S. Prakash, V. Raman, C.F. Lietz, W.A. Hargus, S.A. Schumaker, Numerical simulation of a methane-oxygen rotating detonation rocket engine, P. Combust. Inst. 38 (2021) 3777–3786.

[17] R. Burke, T. Rezzag, I. Dunn, W. Flores, K. Ahmed, The effect of premixed stratification on the wave dynamics of a rotating detonation combustor, Int. J. Hydrogen Energ. 46 (2021) 27816–27826.

[18] W.H. Heiser, D.T. Pratt, Thermodynamic cycle analysis of pulse detonation engines, J. Propul. Power 18 (2002) 68–76.

[19] C.A. Nordeen, D. Schwer, F. Schauer, J. Hoke, T. Barber, B.M. Cetegen, Role of inlet reactant mixedness on the thermodynamic performance of a rotating detonation engine, Shock Waves 26 (2016) 417–428.

[20] M. Zhao, J.M. Li, C.J. Teo, B.C. Khoo, H. Zhang, Effects of Variable Total Pressures on Instability and Extinction of Rotating Detonation Combustion, Flow. Turbul. Combust. 104 (2020) 261–290.

[21] J. Sun, J. Zhou, S. Liu, Z. Lin, J. Cai, Effects of injection nozzle exit width on rotating detonation engine, Acta Astronaut. 140 (2017) 388–401.

[22] R.Zhou, J.P. Wang, Numerical investigation of shock wave reflections near the head ends of rotating detonation engines, Shock Waves 23 (2013) 461–472.

[23] N. Tsuboi, S. Eto, A.K. Hayashi, T. Kojima, Front Cellular Structure and Thrust Performance on Hydrogen–Oxygen Rotating Detonation Engine, J. Propul. Power 33 (2016) 100–111.

[24] N. Tsuboi, N.H. Jourdaine, T. Watanabe, A. Koichi Hayashi, T. Kojima, Three-dimensional numerical simulation on hydrogen-oxygen rotating detonation engine with unchoked aerospike nozzle, AIAA Scitech 2018 Forum, American Institute of Aeronautics and Astronautics (2018), paper AIAA 2018-1885

[25] L.F. Zhang, J.Z. Ma, S.J. Zhang, M.Y. Luan, J.P. Wang, Three-dimensional numerical study on rotating detonation engines using reactive Navier-Stokes equations, Aerosp. Sci. Technol. 93 (2019) paper 105271.

[26] C.F. Lietz, Y. Desai, W. Hargus, V. Sankaran,Parametric investigation of rotating detonation rocket engines using large eddy simulations. AIAA Propulsion and Energy Forum 2019, American Institute of Aeronautics and Astronautics Inc (2019), paper AIAA 2019-4129

[27] J. Sun, J. Zhou, S. Liu, Z. Lin, Numerical investigation of a rotating detonation engine under premixed/non-premixed conditions, Acta Astronaut. 152 (2018) 630–638.

[28] A. Batista, M.C. Ross, C. Lietz, W.A. Hargus, Descending Modal Transition Dynamics in a Large Eddy Simulation of a Rotating Detonation Rocket Engine, Energies (2021) 14 paper 3387.

[29] D. Schwer, K. Kailasanath, Fluid dynamics of rotating detonation engines with hydrogen and hydrocarbon fuels, P. Combust. Inst. 34 (2013) 1991–1998.

[30] J. Sosa, K.A. Ahmed, R. Fievisohn, J. Hoke, T. Ombrello, F. Schauer, Supersonic driven detonation dynamics for rotating detonation engines, Int. J. Hydrogen Energy 44 (2019) 7596–7606.

[31] F. Chacon, M. Gamba, OH PLIF Visualization of an Optically Accessible Rotating Detonation Combustor AIAA Propulsion and Energy Forum 2019, American Institute of Aeronautics and Astronautics Inc (2019), paper AIAA 2019-4217

[32] T. Sato, F. Chacon, L. White, V. Raman, M. Gamba, Mixing and detonation structure in a rotating detonation engine with an axial air inlet, P. Combust. Inst. (2020) 38 3769-3776

[33] V.R. Katta, K.Y. Cho, J.L. Hoke, J.R. Codoni, F.R. Schauer, W.M. Roquemore, Effect of increasing channel width on the structure of rotating detonation wave, P. Combust. Inst. 37 (2019) 3575–3583.

[34] J. Braun, J. Sousa, G. Paniagua, Numerical Assessment of the Convective Heat Transfer in Rotating Detonation Combustors Using a Reduced-Order Model, Appl. Sci. 8 (2018) paper 893.

[35] H. Wen, Q. Xie, B. Wang, Propagation behaviors of rotating detonation in an obround combustor, Combust. Flame 210 (2019) 389–398.

[36] S. Jin, L. Qi, N. Zhao, H. Zheng, Q. Meng, J. Yang, ScienceDirect Experimental and numerical research on rotating detonation combustor under non-premixed conditions, Int. J. Hydrogen Energ. 45 (2019) 10176–10188.

[37] G.C. Mathews, M.G. Blaisdell, A.I. Lemcherfi, C.D. Slabaugh, C.S. Goldenstein, High-bandwidth laser-

absorption measurements of temperature, pressure, CO, and H_2O in the annulus of a rotating detonation rocket engine, AIAA Scitech 2021 Forum, American Institute of Aeronautics and Astronautics (2021), paper AIAA 2021-0418.

[38] B.A. Rankin, D.R. Richardson, A.W. Caswell, A.G. Naples, J.L. Hoke, F.R. Schauer, Chemiluminescence imaging of an optically accessible non-premixed rotating detonation engine, Combust. Flame 176 (2017) 12–22.

[39] B.A. Rankin, J.R. Codoni, K.Y. Cho, J.L. Hoke, F.R. Schauer, Investigation of the structure of detonation waves in a non-premixed hydrogen – air rotating detonation engine using mid-infrared imaging, P. Combust. Inst. 37 (2019) 3479–3486.

[40] D. Dausen, C. Brophy, R. Wright, J. Marder, Design of an Optically-Accessible Rotating Detonation Engine. 48th AIAA/ASME/SAE/ASEE Joint Propulsion Conference & Exhibit, American Institute of Aeronautics and Astronautics Inc (2012), paper AIAA 6.2012-3944.

[41] V. Athmanathan, J.M. Fisher, Z.M. Ayers, D.G. Cuadrado, V. Andreoli, J. Braun, et al.,Turbine-integrated High-pressure Optical RDE (THOR) for injection and detonation dynamics assessment. AIAA Propulsion and Energy Forum 2019, American Institute of Aeronautics and Astronautics Inc (2019), paper AIAA 2019-4041.

[42] X. Huang, C.J. Teo, B.C. Khoo, Experimental investigation on coexisting wave components in an optically accessible rotating detonation combustor, Aerosp. Sci. Technol. 111 (2021) paper 106538.

[43] Jodele, J., Zahn, A., Anand, V., and Gutmark, E., OH* Chemiluminescence Investigation of Rotating Detonation Wave Structure, Proceedings of the 27th International Colloquium on the Dynamics of Explosions and Reactive Systems (2019), Paper 212

[44] B.A. Rankin, C.A. Fugger, D.R. Richardson, K.Y. Cho, J.L. Hoke, A.W. Caswell, J. R. Gord, F. Schauer, Evaluation of Mixing Processes in a Non-Premixed Rotating Detonation Engine Using Acetone PLIF Imaging, AIAA Scitech 2016 Forum, American Institute of Aeronautics and Astronautics (2016), paper AIAA 2016-1198

[45] C. A. Fugger, J. G. Lopez, K. D. Rein, S. Roy, A. W. Caswell, The dynamics of a non-premixed rotating

detonation engine from time-resolved temperature measurements, P. Combust. Inst. 38 (2021) 3787–3795.

[46] C.A. Fugger, K.Y. Cho, J. Hoke, M. G. Gomez, T.R. Meyer, S.A. Schumaker, A. W. Caswell, Detonation Dynamics Visualization From Megahertz Imaging, AIAA Scitech 2020 Forum, American Institute of Aeronautics and Astronautics (2020), paper AIAA 2020-0441

[47] V. Athmanathan, J. Braun, Z. Ayers, J. Fisher, C. Fugger, S. Roy, et al.,Detonation structure evolution in an optically-accessible non-premixed H_2-air RDC using MHz rate imaging. AIAA Scitech 2020 Forum, American Institute of Aeronautics and Astronautics (2020), paper AIAA 2020-1178

[48] J. Jodele, V. Anand, A. Zahn, N. Chiles, E. Gutmark, Quantification of Rotating Detonations Using OH* Chemiluminescence at Varied Widths, AIAA J. 59 (2021) 2457–2466.

[49] K. Matsuoka, M. Tanaka, T. Noda, A. Kawasaki, J. Kasahara, Experimental investigation on a rotating detonation cycle with burned gas backflow, Combust. Flame 225 (2021) 13–19.

[50] L.R. Boeck, F.M. Berger, J. Hasslberger, T. Sattelmayer, Detonation propagation in hydrogen–air mixtures with transverse concentration gradients, Shock Waves 26 (2016) 181–192.

[51] K. Ishii, M. Kojima, Behavior of detonation propagation in mixtures with concentration gradients, Shock Waves 17 (2007) 95–102.

[52] F. Ettner, K.G. Vollmer, T. Sattelmayer, Mach reflection in detonations propagating through a gas with a concentration gradient, Shock Waves 23 (2013) 201–206.

[53] R. Yokoo, K. Goto, J. Kasahara, V. Athmanathan, J. Braun, G. Paniagua, et al., Experimental study of internal flow structures in cylindrical rotating detonation engines, P. Combust. Inst. 38 (2021) 3759–3768.

[54] M. A. Nettleton, Gaseous Detonations - their nature, effects and control., first ed., Springer, London, 1987.

[55] P.S. Hsu, M.N. Slipchenko, N. Jiang, C.A. Fugger, A.M. Webb, V. Athmanathan, T. R. Meyer, S. Roy, Megahertz-rate OH planar laser-induced fluorescence imaging in a rotating detonation combustor, Opt. Lett. 45 (2020) 5776-5779.

[56] R.W. Schefer, W.D. Kulatilaka, B.D. Patterson, T.B. Settersten, Visible emission of hydrogen flames, Combust. Flame 156 (2009) 1234–1241.

[57] C.A. Fugger, P.S. Hsu, N. Jiang, S. Roy, M.N. Slipchenko, V. Athmanathan, A. M. Webb, J. Fisher, T. R.

Meyer, Megahertz OH-PLIF imaging in a Rotating Detonation Engine. AIAA Scitech 2021 Forum, American Institute of Aeronautics and Astronautics (2021), paper AIAA 2021-0555

[58] S. Chakravarthy, O. Peroomian, U. Goldberg, S. Palaniswamy, The CFD++ computational fluid dynamics software suite, World Aviation Congress & Exposition, SAE International (1998), SAE Technical Paper 985564.

[59] J. Braun, G. Paniagua, F. Falempin, B. Le Naour, Design and Experimental Assessment of Bladeless Turbines for Axial Inlet Supersonic Flows, J. Eng. Gas Turb. Power 142 (2020) paper 041024 .

[60] S.M. Frolov, A. V. Dubrovskii, V.S. Ivanov,Three-dimensional numerical simulation of operation process in rotating detonation engine, Progress in Propulsion Physics 4 (2013) 467-488.

[61] X. M. Tang, J. P. Wang, Y. T. Shao, Three-dimensional numerical investigations of the rotating detonation engine with a hollow combustor, Combust. Flame 225 (2015) 997-1008

[62] S. Yao, X. Tang, M. Luan, J. P. Wang Numerical study of hollow rotating detonation engine with different fuel injection area ratios P. Combust. Inst. 34 (2017) 2649-2655.

[63] S. M. Frolov, A. V. Dubrovskii, V. S. Ivanov, Three-dimensional numerical simulation of the operation of a rotating detonation chamber with separate supply of fuel and oxidizer, Russ. J. Phys. Ch. 7 (2013) 35-43

[64] Q. Meng, N. Zhao, H. Zheng, J. Yang, L. Qi, Numerical investigation of the effect of inlet mass flow rates on H2/air non-premixed rotating detonation wave, Int. J. Hydrogen Energ. 43 (2018) 13618-13631.

[65] V. Athmanathan, K.A. Rahman, D.K. Lauriola, J. Braun, G. Paniagua, M.N. Slipchenko, S. Roy, T. R. Meyer, Femtosecond/picosecond rotational coherent anti-Stokes Raman scattering thermometry in the exhaust of a rotating detonation combustor, Combust. Flame 231 (2021), https://doi.org/10.1016/j.combustflame.2021.111504.

[66] D.T. Pratt, J.W. Humphrey, D.E. Glenn, Morphology of standing oblique detonation waves, J. Propul. Power 7 (1991) 837–845.

[67] C. Li, K. Kailasanath, E. S. Oran, Detonation structure behind oblique shocks, Phys. Fluid 6 (1994) 1600–1611

[68] V.R. Katta, T.R. Meyer, M.S. Brown, J.R. Gord, and W.M. Roquemore, “Extinction Criterion for

Unsteady, Opposing-Jet Diffusion Flames," Combust. Flame 137 (1-2), 198-221, 2004.

[69] T. R. Meyer, S. Roy, T. N. Anderson, J. D. Miller, V. R. Katta, R. P. Lucht, J. R. Gord, Measurements of OH mole fraction and temperature up to 20 kHz by using a diode-laser-based UV absorption sensor, Appl. Opt. (44), 6729-6740, 2005.

[70] R. Mevel, J. Melguizo-Gavilanes, L. R. Boeck, J. E. Shepherd, Experimental and numerical study of the ignition of hydrogen-air mixtures by a localized stationary hot surface, Int. J. Heat. Fluid. Fl. (76), 154-169, 2019.

[71] F.A. Bykovskii, S.A. Zhdan, E.F. Vedernikov, Continuous spin detonations, J. Propul. Power 22 (2006) 1204–1216.

[72] C.M. Guirao, R. Knystautas, J.H. Lee, W. Benedick, M. Berman, Hydrogen-air detonations, P. Combust. Inst. 19 (1982) 583–590.

[73] G. Ciccarelli, T. Ginsberg, J. Boccio, C. Economos, K. Sato, M. Kinoshita, Detonation cell size measurements and predictions in hydrogen-air-steam mixtures at elevated temperatures, Combust. Flame 99 (1994) 212–220.